

Direct Imaging and Astrometric Discovery of a Superjovian Planet Orbiting an Accelerating Star

Thayne Currie,^{1,2,3*} G. Mirek Brandt,⁴ Timothy D. Brandt⁴, Brianna Lacy^{5,6}, Adam Burrows⁵, Olivier Guyon^{1,7,8}, Motohide Tamura^{7,9,10}, Ranger Y. Liu¹¹, Sabina Sagynbayeva¹², Taylor Tobin¹³, Jeffrey Chilcote¹³, Tyler Groff¹⁴, Christian Marois^{15,16}, William Thompson¹⁶, Simon Murphy¹⁷, Masayuki Kuzuhara⁷, Kellen Lawson¹⁴, Julien Lozi¹, Vincent Deo¹, Sebastien Vievard¹, Nour Skaf¹, Taichi Uyama¹⁸, Nemanja Jovanovic¹⁹, Frantz Martinache²⁰, N. Jeremy Kasdin²¹, Tomoyuki Kudo¹, Michael McElwain¹⁴, Markus Janson²², John Wisniewski²³, Klaus Hodapp²⁴, Jun Nishikawa^{9,10}, Krzysztof Hełminiak²⁵, Jungmi Kwon¹⁰, Masa Hayashi⁹

¹Subaru Telescope, National Astronomical Observatory of Japan, Hilo, HI, USA

²University of Texas-San Antonio, 1 UTSA Circle, San Antonio, TX, USA

³Eureka Scientific, Oakland, CA, USA

⁴Department of Physics, University of California, Santa Barbara, Santa Barbara, California, USA

⁵Department of Astrophysical Sciences, Princeton University, Princeton, NJ, USA

⁶Department of Astronomy, University of Texas-Austin, Austin, TX, USA

⁷Astrobiology Center, 2-21-1, Osawa, Mitaka, Tokyo, 181-8588, Japan

⁸Steward Observatory, The University of Arizona, Tucson, AZ 85721, USA

⁹National Astronomical Observatory of Japan, 2-21-2, Osawa, Mitaka, Tokyo, Japan

¹⁰Department of Astronomy, Graduate School of Science, The University of Tokyo, Tokyo, Japan

¹¹Parsons School of Design, New York, NY, USA

¹²Department of Physics and Astronomy, State University of New York-Stony Brook, Stony Brook, NY, USA

¹³Department of Physics, University of Notre Dame, Notre Dame, IN, USA

¹⁴NASA-Goddard Space Flight Center, Greenbelt, MD, USA

¹⁵NRC-Herzberg, Victoria, BC, Canada

¹⁶Department of Physics and Astronomy, University of Victoria, Victoria, BC, Canada

¹⁷Centre for Astrophysics, University of Southern Queensland, Toowoomba, QLD 4350, Australia

¹⁸Infrared Processing and Analysis Center, California Institute of Technology, Pasadena, CA, USA

¹⁹Department of Astronomy, California Institute of Technology, Pasadena, CA, USA

²⁰Universite Cote d'Azur, Observatoire de la Cote d'Azur, CNRS, Laboratoire Lagrange, Nice, France

²¹Department of Mechanical Engineering, Princeton University, Princeton, NJ, USA

²²Department of Astronomy, Stockholm University, Stockholm, Sweden

²³Department of Physics and Astronomy, George Mason University, Fairfax, VA USA

²⁴Institute for Astronomy, University of Hawai'i, Hilo, HI, USA

²⁵Nicolaus Copernicus Astronomical Center, Polish Academy of Sciences, Torun, Poland

*To whom correspondence should be addressed; E-mail: currie@naoj.org.

Submitted to Science on February 18, 2022;
Revised Version Passed Independent Peer Review on July 5, 2022

We detect a superjovian extrasolar planet around the dusty A star HIP 99770 using precision astrometry from the *Gaia* and *Hipparcos* satellites and direct imaging using the Subaru Coronagraphic Extreme Adaptive Optics Project. HIP 99770 b is the first exoplanet ever discovered jointly through direct imaging and precision astrometry and the first discovery leveraging on μ -arcsecond precision *Gaia* astrometry. HIP 99770 b is in a low-eccentricity orbit ~ 16.9 au from the primary, receiving about as much light as Jupiter does from the Sun. The planet induces an astrometric acceleration on the host star; its directly-measured companion-to-primary mass ratio is similar to that of many radial-velocity detected planets and some of the first imaged exoplanets, including HR 8799 cde. The planet’s spectrum reveals an atmosphere resembling a slightly less cloudy and likely older analogue of these first imaging discoveries, enabling a new, critical probe of how gas giant planets evolve with time.

HIP 99770 b’s discovery is a direct proof-of-concept for a fundamentally new strategy for finding imageable planets: selecting targets based on dynamical evidence from indirect methods like astrometry instead of conducting blind searches. This combined approach prefigures the campaigns that could one day directly detect and characterize an extrasolar Earth-like planet.

One sentence summary: HIP 99770 b is the first exoplanet jointly discovered through direct imaging and precision astrometry: a proof-of-concept for a fundamentally new approach for finding imageable exoplanets, including exo-Earths with future telescopes.

Introduction

Over the past 13 years, adaptive optics-assisted ground based telescopes have provided the first direct imaging discoveries of extrasolar planets (1–6), a key step towards imaging and characterizing the atmosphere of another Earth. These discoveries draw from *blind* surveys, where targets are selected based on system properties like age and distance. Unfortunately, the low yields of blind surveys show that currently imageable exoplanets are rare (7). Direct imaging provides exceptional constraints on exoplanet atmospheres (8). However, masses for imaged exoplanets are almost never directly measured but instead inferred through luminosity evolution models that are intrinsically uncertain and rely on difficult-to-constrain stellar ages (9, 10). The typically short time baselines and wide separations of imaged exoplanets can also leave orbital parameters derived purely from imaging highly uncertain (11).

Instead of conducting blind searches, coupling direct imaging searches with another indirect detection method can in principle radically improve discovery yields and simultaneously

explore the atmospheres, orbits, and masses for a large population of exoplanets. Astrometric monitoring can identify stars undergoing a proper motion acceleration caused by an unseen but imageable companion, including young stars unsuitable for precise RV measurements (12). Combining the imaged planet’s relative astrometry with absolute astrometry of the star yields precise, directly-determined companion masses and improved constraints on orbital properties (12, 13). The micro-arcsecond precision of the European Space Agency’s *Gaia* mission combined with measurements 20+ years prior from its predecessor, *Hipparcos*, makes possible the astrometric detection of superjovian planets at Jupiter-to-Neptune like separations around the nearest stars for the first time (14).

Target Properties and Data

HIP 99770 (HD 192640; 29 Cyg) is a chemically-peculiar A-type star with an effective temperature of ≈ 8000 K, luminosity of $\approx 13.9 L_{\odot}$, and mass of $\approx 1.7\text{--}2.0 M_{\odot}$ located ~ 40.74 pc from the Sun (Table 1). It is likely either ~ 40 Myr or 115–414 Myr old, depending on whether its kinematics or Hertzsprung-Russell (HR) diagram position is used to assess age. The star is surrounded by a luminous cold, Kuiper belt-like debris disk on > 150 au scales. See Supplemental Material for more details.

We searched for evidence that HIP 99770 shows an astrometric acceleration due to an unseen companion: a deviation from linear motion across the sky. We used astrometry from the *Hipparcos-Gaia Catalogue of Accelerations* (HGCA) (15), a cross-calibration of the *Hipparcos* and *Gaia* missions. HIP 99770’s average proper motion—its position difference over the ≈ 25 years between the *Hipparcos* and *Gaia* missions—differs from the proper motion measured around 2016 by *Gaia* EDR3 (16). HGCA yields $\chi^2 \sim 7.23$ for constant linear motion, revealing a significant acceleration (≈ 2.2 Gaussian sigma) with a false positive rate of 2.7%. The astrometric acceleration provides a lower limit to the ratio $M_{\text{sec}}/R_{\text{sec}}^2$, and suggests a $\approx 11 M_{\text{Jup}}$ companion at a fiducial separation of $0''.5$ (≈ 20 au). Previous high-contrast imaging observations rule out a stellar/substellar companion at wide ($\rho > 1''$) separations (see Supplemental Material), strongly hinting that HIP 99770’s companion orbits closer in and has a lower mass.

We observed HIP 99770 with SCEXAO coupled to the Coronagraphic High-Resolution Imager and Spectrograph (CHARIS), in low-resolution (broadband) mode in 22 spectral channels covering the major near-infrared (IR) passbands simultaneously ($\lambda = 1.16\text{--}2.37 \mu\text{m}$) (17, 18). Our first two data sets consisted of two shallow observing sequences in July and September 2020. Between May and October 2021, we conducted three deeper follow-up SCEXAO/CHARIS observations and obtained one complementary data set in the thermal IR (L_p , $\lambda = 3.78 \mu\text{m}$) with the NIRC2 camera on the Keck II Telescope.

SCEXAO/CHARIS reveals a faint point source, hereafter HIP 99770 b, located $\rho \sim 0.43''\text{--}0.44''$ southeast of its host star (Figure 1; Table 1). In the highest-quality data, HIP 99770 b is visible across the entire spectral range using advanced PSF subtraction methods combined with different observing/residual noise suppression strategies (Figure 2, left panel). Each CHARIS

data set shows a clear detection, establishing an astrometric baseline longer than one year (middle panel). We also recover HIP 99770 b in Keck/NIRC2 thermal IR data (right panel).

Analysis

Our astrometry easily rejects HIP 99770 b being a background object at the $>15\text{-}\sigma$ level. Between our first epoch (29 July 2020) and fourth epoch (13 July 2021), a background star should appear to move by ~ 65 mas to both the west and south (Table 1) due to the star’s proper motion. However, over this time baseline HIP 99770 b moved 23 ± 6 mas to the east and 29 ± 6 mas to the north: i.e. in the *opposite* direction expected for a background star.

To determine HIP 99770 b’s orbital properties and mass, we simultaneously fit its relative astrometry (from imaging data) and the primary’s proper motions and anomalies (from the HGCA) using `orvara` (19). We adopted the standard uninformative priors discussed in (20), but use a more conservative uniform prior on the companion mass and a Gaussian $1.8 \pm 0.2 M_\odot$ prior on the primary. We performed additional tests adopting a $1/M_p$ companion prior and changing the prior for the primary mass (see Supplemental Material); these changes have little effect on our results.

The posterior distributions from `orvara` for HIP 99770 b’s orbital parameters constrain key properties (Figure 3). We derive a semimajor axis of $16.9^{+3.4}_{-1.9}$ au: comparable to HR 8799 e’s orbit (21). HIP 99770 b’s eccentricity is low, $e = 0.25^{+0.14}_{-0.16}$: more similar to values for directly imaged planets than brown dwarfs (11).

HIP 99770 b has a dynamical mass of $16.1^{+5.4}_{-5.0} M_J$, for a mass ratio of $q = (8.7 \pm 2.9) \times 10^{-3}$. Adopting a $1/M_p$ prior on the companion mass instead of a linear prior yields a mass of $13.9^{+6.1}_{-5.1} M_J$ ($q = (7.7 \pm 3.1) \times 10^{-3}$). HIP 99770 b’s mass is lower than the local minimum in values empirically separating massive planets from brown dwarfs (see Supplemental Material). HIP 99770 b’s mass ratio is intermediate between mass ratios measured for some exoplanets like HR 8799 e ($q \approx 6 \times 10^{-3}$) and those inferred for other, wider-separation exoplanets like TYC 8998-760-1 b ($q \approx 0.01\text{--}0.015$) but is much lower than mass ratios measured for the brown dwarfs GJ 758 B and HD 33632 Ab ($q > 0.04$) (4, 20–22).

Comparing HIP 99770 b’s CHARIS spectrum to a library of substellar object spectra and spectral standards provides a first, coarse estimate of its temperature (23, 24). These comparisons show that HIP 99770 b lies at the critical transition from cloudy, methane poor L-type substellar objects to (nearly) cloud-free, T-type objects showing methane absorption (the “L/T transition”). The L7 field dwarf template best reproduces its spectrum amongst all spectral standards. In the spectral library, the L9.5 field dwarf SIMPJ0956-1447 best fits HIP 99770 b. Thus, we assign HIP 99770 b a spectral type of L7–L9.5, which corresponds to a likely effective temperature of $T_{\text{eff}} \sim 1300\text{--}1500$ K (25). HIP 99770 b’s atmosphere appears intermediate between SIMPJ0956-1447 and the directly imaged, extremely cloudy L/T transition exoplanet HR 8799 d (Figure 4, top panel).

We further characterize HIP 99770 b’s atmosphere, comparing its CHARIS spectrum and

NIRC2 photometry to multiple grids of atmospheric models spanning a range of temperatures and gravities and adopting different prescriptions for clouds and atmospheric dust. Atmospheric models require clouds to match HIP 99770 b’s spectrum, although the planet is likely less cloudy/dusty than the HR 8799 planets. The best-fitting models cover $\log(g) = 4\text{--}4.25$ and temperature of 1450 K (Figure 4, bottom panel; Supplemental Material); well-fitting models have $\log(g) = 4\text{--}4.5$ and temperatures of $1300\text{--}1500\text{ K}$. HIP 99770 b’s range of best-fitting temperatures and radii yield a luminosity of $\log(L/L_\odot) = -4.55 \pm 0.02$, or a luminosity ratio of 2×10^{-6} relative to the primary. Masses inferred from luminosity evolution are consistent with the planet’s dynamical mass if the system is $\sim 80\text{--}200\text{ Myr}$ old (see Supplemental Materials).

The architecture of the HIP 99770 planetary system draws comparisons to the solar system. HIP 99770 b orbits at $\sim 16.9\text{ au}$, intermediate between the distances of Saturn and Uranus from the Sun. The system’s cold debris disk is likely $>150\text{ au}$ from the star, about 3.5 times the typical distance from the Sun to Kuiper belt objects. However, the insolation for HIP 99770 b is comparable to that at $\sim 4.5\text{ au}$ in the solar system, very close to the orbit of Jupiter. Likewise, HIP 99770’s debris disk, if at 150 au , lies at a luminosity-scaled distance comparable to that of the Kuiper belt from the Sun. Thus, like HR 8799, HIP 99770 bears some characteristics of a scaled-up version of our own solar system, albeit one where a single massive planet dominates.

The mass ratios (q) and separations (a_p) of substellar companions provide a coarse diagnostic of formation processes. Surveys suggest that the companion mass function for substellar objects reaches a local minimum at $q \sim 0.025$ where small (large) q values better probe planets formed in a disk (brown dwarf companions formed by fragmentation) (26). Stellar companions formed through fragmentation have q values as small as 0.08 (27). As with a few other RV-detected companions orbiting stars more massive than the Sun with masses at or slightly above the deuterium-burning limit, HIP 99770 b’s mass ratio and separation ($q \sim 0.0087$, $a_p \sim 16.9\text{ au}$) is contiguous with planets below the deuterium-burning limit detected by both direct imaging and RV (Figure 5). Supplemental Material discusses the taxonomy of companions in more detail and shows why HIP 99770 b is also contiguous with the planet population, not brown dwarfs, in terms of mass.

Significance

HIP 99770 b is the first extrasolar planet jointly discovered through direct and indirect techniques: direct imaging and precision astrometry. HIP 99770 b joins $\beta\text{ Pic bc}$ and HR 8799 e as the only imaged planets with both spectra and dynamical masses. Analysis combining dynamics and luminosity evolution suggests that HIP 99770 b is older than these planets. A precise, directly-constrained age for the HIP 99770 primary – e.g. from future CHARA interferometry – will solidify HIP 99770 b as a critical benchmark for understanding planet atmospheric evolution.

HIP 99770 b also provides a potentially key test of direct imaging technologies. The *Roman Space Telescope* Coronagraphic Instrument (CGI) technological demonstration is a key stepping

stone to image an Earth-like planet with a future flagship mission and requires demonstrating a contrast deeper than 10^{-7} at $\lambda_c \leq 600$ nm ($>10\%$ bandpass) located $6-9 \lambda/D$ ($\sim 0.3''-0.45''$) from a very bright ($V_{AB} \leq 5$) star. Current best-estimated performance predicts a contrast of $\sim 10^{-9}$ over this range. Our best-fit orbit places HIP 99770 b at $[E,N]'' = [0.358, -0.137] \pm [0.025, 0.024]$, $[0.354, -0.040] \pm [0.043, 0.035]$, and $[0.325, 0.058] \pm [0.072, 0.045]$ on dates covering CGI's likely performance period (July 1 2026, July 1 2028, and July 1 2030, respectively). We predict HIP 99770 b's contrast in CGI's band 1 centered on 575 nm to be 1.7×10^{-10} to 2.3×10^{-9} and depending primarily on clouds/atmospheric dust and surface gravity. For a subset of solutions, HIP 99770 b would be imageable by CGI at 575 nm and thus suitable for the CGI technological demonstration. At longer wavelengths (660 nm–730 nm), HIP 99770 b's contrast is milder ($\sim 10^{-8}-10^{-7}$) and should be detectable with CGI spectroscopy. Provided that CGI performs as expected, HIP 99770 could be an excellent test of ultra-deep contrasts from space and exoplanet spectroscopic characterization in the optical. See Supplemental Material for more details.

Finally, HIP 99770 b is a proof-of-concept a fundamentally different approach for finding imageable planets: conducting a *targeted*, dynamics-selected search for young Jupiters instead of a blind survey. Early results from our pilot accelerating star program suggest a discovery yield substantially higher than blind surveys conducted with comparably powerful instruments (28). The need to select imaging targets through either precision astrometry or extreme-precision RV will be potentially even more important for the efficient direct detection of short-period, Earth and Jupiter-like planets in reflected light on the ground with future facilities like the *Thirty Meter Telescope* or in space with the NASA direct imaging flagship mission endorsed by the Astro 2020 Decadal Survey or highlighted in the European Space Agency's Voyage 2050 report (29).

References

1. C. Marois, B. Zuckerman, Q. M. Konopacky, B. Macintosh, T. Barman, *Nature* **468**, 1080 (2010).
2. A.-M. Lagrange, *et al.*, *Science* **329**, 57 (2010).
3. J. Carson, *et al.*, *ApJL* **763**, L32 (2013).
4. T. Currie, *et al.*, *ApJL* **780**, L30 (2014).
5. B. Macintosh, *et al.*, *Science* **350**, 64 (2015).
6. G. Chauvin, *et al.*, *A&A* **605**, L9 (2017).
7. E. L. Nielsen, *et al.*, *AJ* **158**, 13 (2019).
8. Q. M. Konopacky, T. S. Barman, B. A. Macintosh, C. Marois, *Science* **339**, 1398 (2013).

9. D. S. Spiegel, A. Burrows, *ApJ* **745**, 174 (2012).
10. M. Bonnefoy, *et al.*, *A&A* **618**, A63 (2018).
11. B. P. Bowler, S. C. Blunt, E. L. Nielsen, *AJ* **159**, 63 (2020).
12. T. D. Brandt, T. J. Dupuy, B. P. Bowler, *AJ* **158**, 140 (2019).
13. I. A. G. Snellen, A. G. A. Brown, *Nature Astronomy* **2**, 883 (2018).
14. M. Perryman, J. Hartman, G. Á. Bakos, L. Lindegren, *ApJ* **797**, 14 (2014).
15. T. D. Brandt, *ApJS* **254**, 42 (2021).
16. Gaia Collaboration, *et al.*, *A&A* **649**, A1 (2021).
17. N. Jovanovic, *et al.*, *PASP* **127**, 890 (2015).
18. T. D. Groff, *et al.*, *Ground-based and Airborne Instrumentation for Astronomy VI* (2016), vol. 9908 of *Society of Photo-Optical Instrumentation Engineers (SPIE) Conference Series*, p. 99080O.
19. T. D. Brandt, *et al.*, *AJ* **162**, 186 (2021).
20. G. M. Brandt, *et al.*, *arXiv e-prints* p. arXiv:2109.07525 (2021).
21. G. M. Brandt, T. D. Brandt, T. J. Dupuy, D. Michalik, G.-D. Marleau, *ApJL* **915**, L16 (2021).
22. A. J. Bohn, *et al.*, *ApJL* **898**, L16 (2020).
23. J. Gagné, D. Lafrenière, R. Doyon, L. Malo, É. Artigau, *ApJ* **783**, 121 (2014).
24. K. L. Cruz, *et al.*, *AJ* **155**, 34 (2018).
25. D. C. Stephens, *et al.*, *ApJ* **702**, 154 (2009).
26. M. Reggiani, *et al.*, *A&A* **586**, A147 (2016).
27. M. Bonavita, *et al.*, *arXiv e-prints* p. arXiv:2103.13706 (2021).
28. T. Currie, *et al.*, *Society of Photo-Optical Instrumentation Engineers (SPIE) Conference Series* (2021), vol. 11823 of *Society of Photo-Optical Instrumentation Engineers (SPIE) Conference Series*, p. 1182304.
29. J. P. Greco, A. Burrows, *ApJ* **808**, 172 (2015).
30. S. J. Murphy, E. Paunzen, *MNRAS* **466**, 546 (2017).

31. J. W. Jones, The ages of A-stars, Ph.D. thesis, Georgia State University, United States (2016).
32. F. Royer, J. Zorec, A. E. Gómez, *A&A* **463**, 671 (2007).
33. T. Currie, *et al.*, *ApJL* **760**, L32 (2012).
34. C. Marois, D. Lafrenière, R. Doyon, B. Macintosh, D. Nadeau, *ApJ* **641**, 556 (2006).
35. W. B. Sparks, H. C. Ford, *ApJ* **578**, 543 (2002).
36. A. Z. Greenbaum, *et al.*, *AJ* **155**, 226 (2018).
37. A. Zurlo, *et al.*, *A&A* **587**, A57 (2016).
38. F. Allard, D. Homeier, B. Freytag, *Philosophical Transactions of the Royal Society of London Series A* **370**, 2765 (2012).
39. N. Madhusudhan, A. Burrows, T. Currie, *ApJ* **737**, 34 (2011).
40. G. T. van Belle, K. von Braun, *ApJ* **694**, 1085 (2009).
41. A. Slettebak, *ApJ* **115**, 575 (1952).
42. R. O. Gray, *AJ* **95**, 220 (1988).
43. J. A. Cardelli, G. C. Clayton, J. S. Mathis, *ApJ* **345**, 245 (1989).
44. M. J. Pecaut, E. E. Mamajek, *ApJS* **208**, 9 (2013).
45. R. Lallement, B. Y. Welsh, J. L. Vergely, F. Crifo, D. Sfeir, *A&A* **411**, 447 (2003).
46. W. Reis, W. Corradi, M. A. de Aveliz, F. P. Santos, *ApJ* **734**, 8 (2011).
47. B. Zuckerman, J. H. Rhee, I. Song, M. S. Bessell, *ApJ* **732**, 61 (2011).
48. B. Zuckerman, *ApJ* **870**, 27 (2019).
49. Gaia Collaboration, *et al.*, *A&A* **616**, A10 (2018).
50. J. Jones, *et al.*, *ApJ* **813**, 58 (2015).
51. S. J. Murphy, M. Joyce, T. R. Bedding, T. R. White, M. Kama, *MNRAS* **502**, 1633 (2021).
52. T. R. Bedding, *et al.*, *Nature* **581**, 147 (2020).
53. S. J. Murphy, *et al.*, *arXiv e-prints* p. arXiv:2111.04203 (2021).
54. M. Asplund, N. Grevesse, A. J. Sauval, P. Scott, *ARA&A* **47**, 481 (2009).

55. L. M. Rebull, *et al.*, *ApJ* **681**, 1484 (2008).
56. J. Milli, *et al.*, *Adaptive Optics Systems VI*, L. M. Close, L. Schreiber, D. Schmidt, eds. (2018), vol. 10703 of *Society of Photo-Optical Instrumentation Engineers (SPIE) Conference Series*, p. 107032A.
57. T. Currie, *et al.*, *AJ* **156**, 291 (2018).
58. T. Currie, *et al.*, *Society of Photo-Optical Instrumentation Engineers (SPIE) Conference Series* (2020), vol. 11448 of *Society of Photo-Optical Instrumentation Engineers (SPIE) Conference Series*, p. 114487H.
59. C. Marois, R. Doyon, R. Racine, D. Nadeau, *PASP* **112**, 91 (2000).
60. N. Jovanovic, *et al.*, *The Astrophysical Journal Letters* **813**, L24 (2015).
61. T. D. Brandt, *et al.*, *Journal of Astronomical Telescopes, Instruments, and Systems* **3**, 048002 (2017).
62. T. Currie, *et al.*, *ApJ* **729**, 128 (2011).
63. T. Currie, *et al.*, *ApJL* **814**, L27 (2015).
64. D. Lafrenière, C. Marois, R. Doyon, D. Nadeau, É. Artigau, *ApJ* **660**, 770 (2007).
65. C. Marois, B. Macintosh, J.-P. Véran, *Proc. SPIE* (2010), vol. 7736 of *Society of Photo-Optical Instrumentation Engineers (SPIE) Conference Series*, p. 77361J.
66. R. Soummer, L. Pueyo, J. Larkin, *ApJL* **755**, L28 (2012).
67. L. Pueyo, *ApJ* **824**, 117 (2016).
68. E. L. Nielsen, *et al.*, *ApJ* **750**, 53 (2012).
69. J. P. Greco, T. D. Brandt, *ApJ* **833**, 134 (2016).
70. R. Galicher, *et al.*, *A&A* **594**, A63 (2016).
71. W. Thompson, C. Marois, *AJ* **161**, 236 (2021).
72. A. Burrows, D. Sudarsky, I. Hubeny, *ApJ* **640**, 1063 (2006).
73. J. Tennyson, *et al.*, *Journal of Molecular Spectroscopy* **327**, 73 (2016).
74. K. L. Chubb, *et al.*, *A&A* **646**, A21 (2021).
75. E. Gharib-Nezhad, *et al.*, *ApJS* **254**, 34 (2021).

76. N. F. Allard, F. Spiegelman, J. F. Kielkopf, *A&A* **589**, A21 (2016).
77. N. F. Allard, F. Spiegelman, T. Leininger, P. Molliere, *A&A* **628**, A120 (2019).
78. I. Hubeny, A. Burrows, *ApJ* **669**, 1248 (2007).
79. T. S. Barman, B. Macintosh, Q. M. Konopacky, C. Marois, *ApJL* **735**, L39 (2011).
80. I. Baraffe, G. Chabrier, T. S. Barman, F. Allard, P. H. Hauschildt, *A&A* **402**, 701 (2003).
81. B. Lacy, A. Burrows, *ApJ* **892**, 151 (2020).
82. G. Gatewood, H. Eichhorn, *AJ* **78**, 769 (1973).
83. J. L. Bean, *et al.*, *ApJL* **711**, L19 (2010).
84. M. W. Muterspaugh, *et al.*, *AJ* **140**, 1657 (2010).
85. J. Sahlmann, *et al.*, *A&A* **565**, A20 (2014).
86. A. Venner, L. A. Pearce, A. Vanderburg, *arXiv e-prints* p. arXiv:2111.03676 (2021).
87. M. J. Pecaut, E. E. Mamajek, E. J. Bubar, *ApJ* **746**, 154 (2012).
88. E. E. Mamajek, C. P. M. Bell, *MNRAS* **445**, 2169 (2014).
89. T. J. Dupuy, *et al.*, *Research Notes of the American Astronomical Society* **4**, 54 (2020).
90. C. Marois, *et al.*, *Science* **322**, 1348 (2008).
91. J. J. Wang, *et al.*, *AJ* **156**, 192 (2018).
92. J. Milli, *et al.*, *A&A* **597**, L2 (2017).
93. T. Currie, *et al.*, *ApJL* **877**, L3 (2019).
94. A. Niedzielski, G. Nowak, M. Adamów, A. Wolszczan, *ApJ* **707**, 768 (2009).
95. L. J. Rosenthal, *et al.*, *ApJS* **255**, 8 (2021).
96. K. Wagner, *et al.*, *ApJL* **902**, L6 (2020).
97. S. Hinkley, *et al.*, *ApJL* **806**, L9 (2015).
98. M. Kuzuhara, *et al.*, *ApJ* **774**, 11 (2013).
99. Q. M. Konopacky, *et al.*, *ApJL* **829**, L4 (2016).
100. D. S. Spiegel, A. Burrows, J. A. Milsom, *ApJ* **727**, 57 (2011).

101. K. M. Kratter, R. A. Murray-Clay, A. N. Youdin, *ApJ* **710**, 1375 (2010).
102. J. Sahlmann, *et al.*, *A&A* **525**, A95 (2011).
103. G. Chabrier, *et al.*, *Protostars and Planets V*, B. Reipurth, D. Jewitt, K. Keil, eds. (2007), p. 623.
104. K. L. Luhman, *Extreme Solar Systems*, D. Fischer, F. A. Rasio, S. E. Thorsett, A. Wolzszczan, eds. (2008), vol. 398 of *Astronomical Society of the Pacific Conference Series*, p. 357.
105. K. Todorov, K. L. Luhman, K. K. McLeod, *ApJL* **714**, L84 (2010).
106. M. C. Liu, *et al.*, *ApJL* **777**, L20 (2013).
107. A. Quirrenbach, T. Trifonov, M. H. Lee, S. Reffert, *A&A* **624**, A18 (2019).
108. D. Grether, C. H. Lineweaver, *ApJ* **640**, 1051 (2006).
109. S. Udry, *In the Spirit of Lyot 2010*, A. Boccaletti, ed. (2010), p. E11.
110. F. Kiefer, *et al.*, *A&A* **631**, A125 (2019).
111. S. M. Andrews, J. P. Williams, *ApJ* **659**, 705 (2007).
112. J. P. Williams, L. A. Cieza, *ARA&A* **49**, 67 (2011).
113. A. L. Kraus, M. J. Ireland, F. Martinache, J. P. Lloyd, *ApJ* **679**, 762 (2008).
114. T. J. Dupuy, M. C. Liu, *ApJS* **201**, 19 (2012).

Acknowledgments

We thank the Subaru Time Allocation committee, NASA-Keck Time Allocation Committee, and Subaru Director Michitoshi Yoshida for their support of this program through Open Use and Director’s Discretionary Time allocations. This research is based on data collected at Subaru Telescope, which is operated by the National Astronomical Observatory of Japan. The authors acknowledge the very significant cultural role and reverence that the summit of Maunakea holds within the Hawaiian community. We are most fortunate to have the opportunity to conduct observations from this mountain. We thank Jonathan Gagne, Eric Mamajek, Richard Gray, and Jeremy Jones for extensive and helpful conversations regarding HIP 99770 A’s spectral type, mass, and age. This work was partially funded under NASA/XRP program NNX17AF88G and NASA-Keck Principal Investigator Award (Program 2020A_N027). We acknowledge the support of the Natural Sciences and Engineering Research Council of Canada (NSERC). The development of SCEXAO was supported by the Japan Society for the Promotion of Science

(Grant-in-Aid for Research #23340051, #26220704, #23103002, #19H00703 and #19H00695), the Astrobiology Center of the National Institutes of Natural Sciences, Japan, the Mt Cuba Foundation and the director's contingency fund at Subaru Telescope.

Table 1: HIP 99770 Planetary System Data

HIP 99770 A			
Property		Value	References
T_{eff}		8000 K	(30) ^a
Spectral Type		kA1.5hA7mA0.5 λ Boo (A5–A6)	(30) ^a
Mass		$1.85 \pm 0.19 M_{\odot}$	(31), this work
Rotation Rate (Projected)		65 km s^{-1}	(32)
Apparent Luminosity		$13.86^{+2.14}_{-5.46} L_{\odot}$	this work
Age		40 Myr, 115-414 Myr	this work
Distance		$40.74 \pm 0.15 \text{ pc}$	(16)
Proper Motion (Gaia-eDR3)		$68.09 \pm 0.12, 69.40 \pm 0.14 \text{ mas yr}^{-1}$	(15, 16)
Proper Motion (H-G scaled)		$68.24 \pm 0.01, 69.67 \pm 0.01 \text{ mas yr}^{-1}$	(15, 16)
Proper Motion (Hipparcos)		$69.45 \pm 0.38, 69.19 \pm 0.38 \text{ mas yr}^{-1}$	(15, 16)
Proper Motion Anomaly (χ^2)		7.23	(15)
J,H,Ks,L _p		$4.49 \pm 0.05, 4.46 \pm 0.02, 4.42 \pm 0.02, 4.40 \pm 0.05$	this work ^b
HIP 99770 b			
Relative Astrometry			
Date	Instrument	Position [E,N]''	SNR (ADI, ASDI)
20200729	SCExAO/CHARIS	$[0.263,-0.367] \pm [0.004,0.005]$	5.2, 11.3
20200901	SCExAO/CHARIS	$[0.263,-0.366] \pm [0.005,0.005]$	7.3, 16.3
20210519	SCExAO/CHARIS	$[0.280,-0.343] \pm [0.004,0.004]$	17.3, 39.4
20210603	Keck/NIRC2	$[0.286,-0.337] \pm [0.006,0.006]$	11
20210713	SCExAO/CHARIS	$[0.286,-0.338] \pm [0.004,0.004]$	11.7, 22.8
20211017	SCExAO/CHARIS	$[0.292,-0.327] \pm [0.004,0.004]$	24.9, 45.0
Photometric, Spectroscopic, and Orbital Properties			
m_J (1.25 μm)		17.39 ± 0.19	
m_H (1.65 μm)		16.51 ± 0.11	
m_{K_s} (2.16 μm)		15.66 ± 0.09	
m_{L_p} (3.78 μm)		14.52 ± 0.12	
Spectral Type		L7-L9.5	
T_{eff}		$1400^{+200}_{-100} \text{ K}$	
$\log(L/L_{\odot})$		-4.55 ± 0.02	
$\log(g)$		4–5	
Mass		$16.1^{+5.4}_{-5.1} M_J^c$	
Mass Ratio (q)		$0.0087^{+0.0029}_{-0.0029} c$	
a_p		$16.9^{+3.4}_{-1.9} \text{ au}$	
e		$0.25^{+0.14}_{-0.16}$	
i		$148^{+13}_{-11}^{\circ}$	
Predicted contrast (575nm)		$1.7 \times 10^{-10} \text{--} 2.3 \times 10^{-9}$	
Predicted contrast (660nm)		$7.9 \times 10^{-9} \text{--} 2.9 \times 10^{-8}$	
Predicted contrast (730nm)		$6.7 \times 10^{-8} \text{--} 9.4 \times 10^{-8}$	

Notes - a) See Supplemental Materials. b) The star is unsaturated in 2MASS K_s band. We estimated its J , H , and L_p photometry assuming the colors of an A5V star. c) Adopting a $1/M_p$ prior, the mass and mass ratio change to $M_p = 13.9^{+6.1}_{-5.1} M_J$ and $q = 0.0077^{+0.0031}_{-0.0031}$.

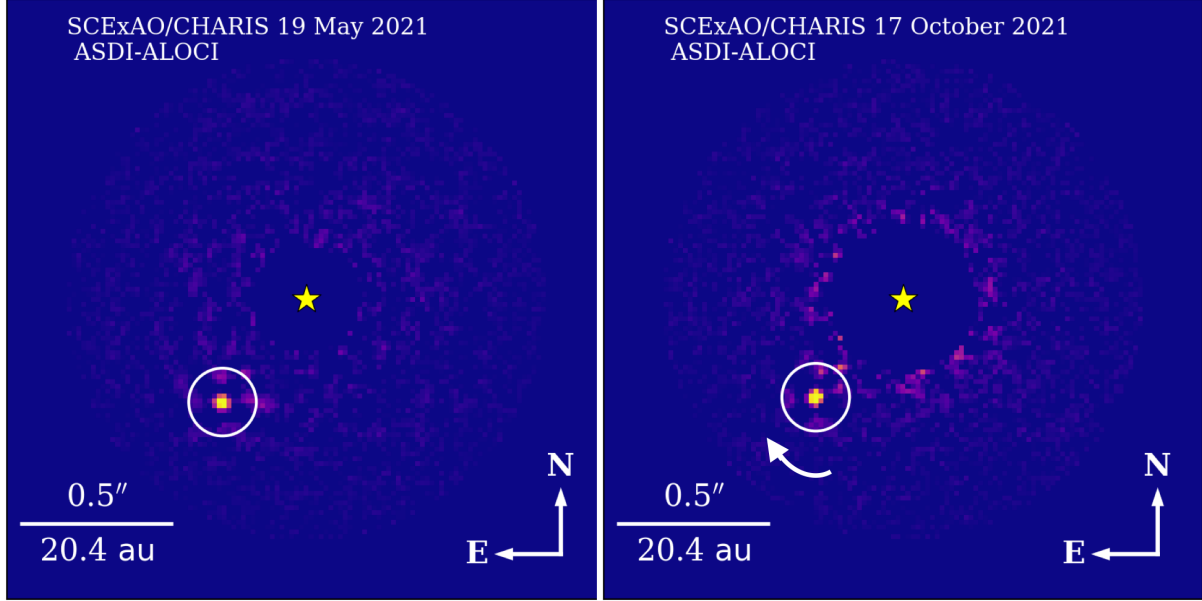


Figure 1: High signal-to-noise ratio detections of HIP 99770 b with SCEXAO/CHARIS from 19 May 2021 and 17 October 2021: our two highest-quality data sets. We used the ALOCI algorithm in combination of *angular differential imaging* (ADI) and *spectral differential imaging* (SDI) (ASDI) to remove the stellar halo light (33–35). The curved arrow in the right panel shows the direction of HIP 99770 b’s motion on the sky. The color intensity scalings are linear with a minimum of zero and maximum scaled to the mean signal within a PSF core.

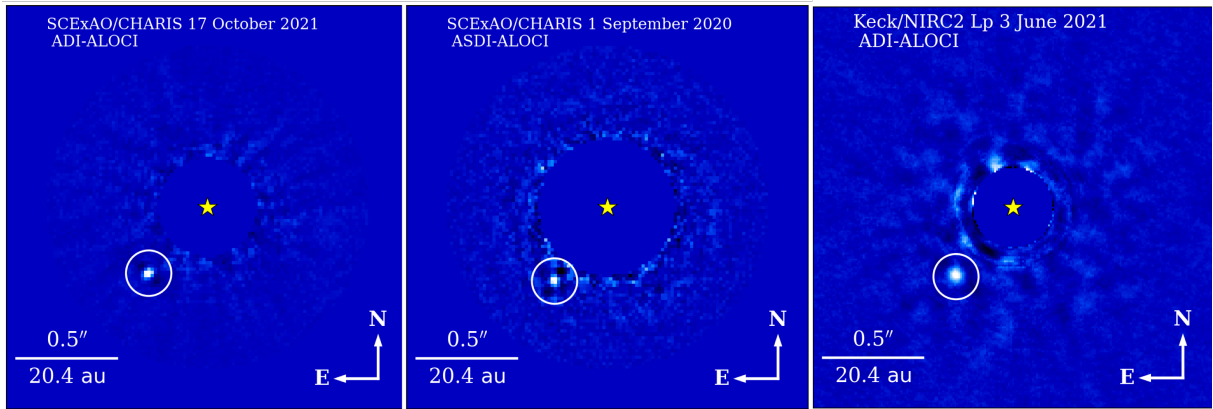


Figure 2: Additional detections of HIP 99770 b used for characterization. (left) The 17 October 2021 data reduced with ADI used to extract a robust planet spectrum. (middle) One of two HIP 99770 b detections from 2020 to lengthen the astrometric baseline. (right) Detection of HIP 99770 b from Keck/NIRC2 thermal IR imaging to extend the planet’s wavelength coverage for atmospheric characterization.

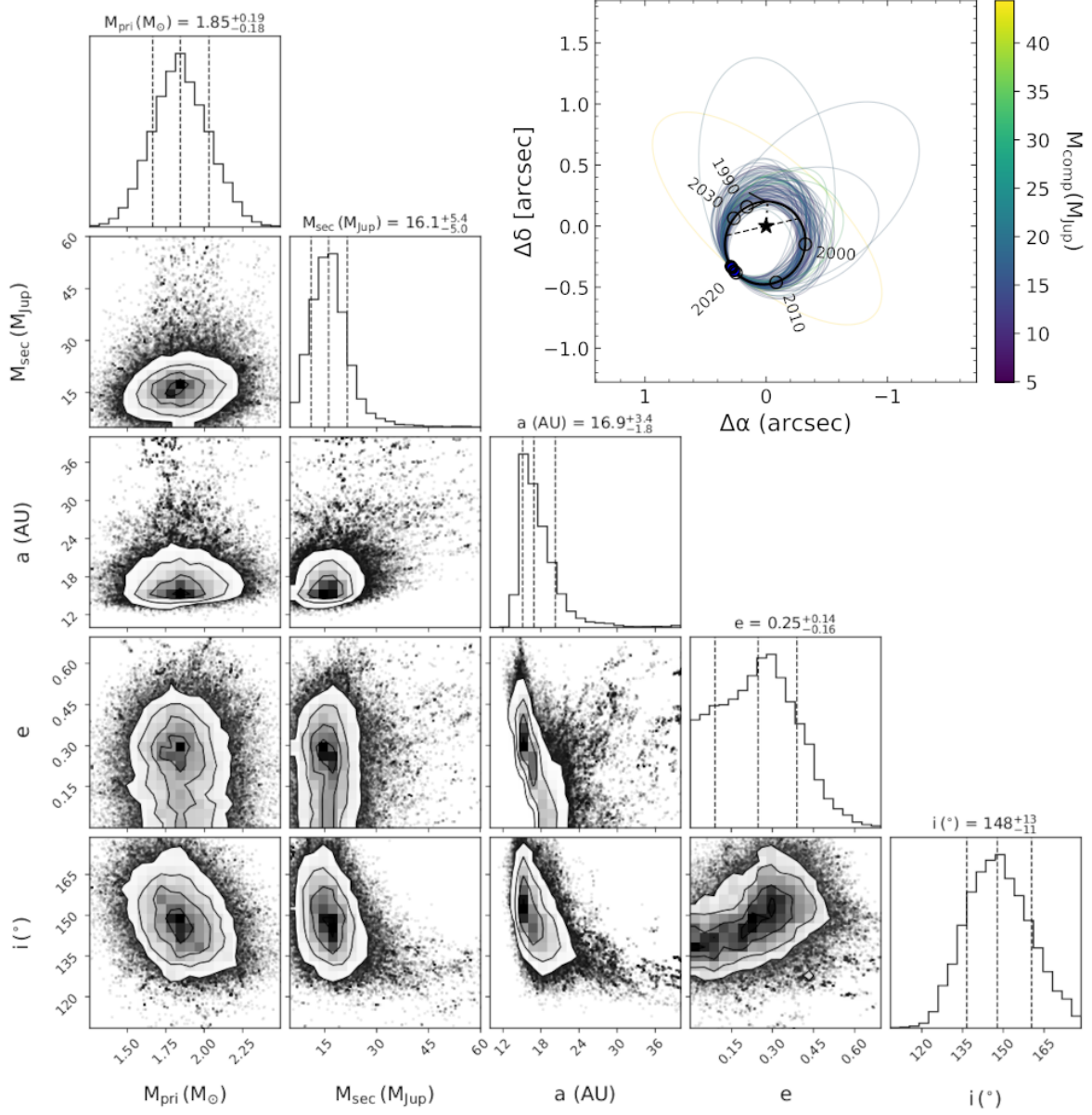


Figure 3: Corner plot showing posterior distributions of selected orbital parameters. The orbit fits used *Hipparcos* and *Gaia* absolute astrometry for HIP 99770 A and relative astrometry of HIP 99770 b. The posterior on HIP 99770 A's mass is similar to our adopted prior of $1.8 \pm 0.2 M_{\odot}$. The inset displays the best-fit orbit along with 100 orbits drawn from our MCMC posterior, color-coded by HIP 99770 b's mass.

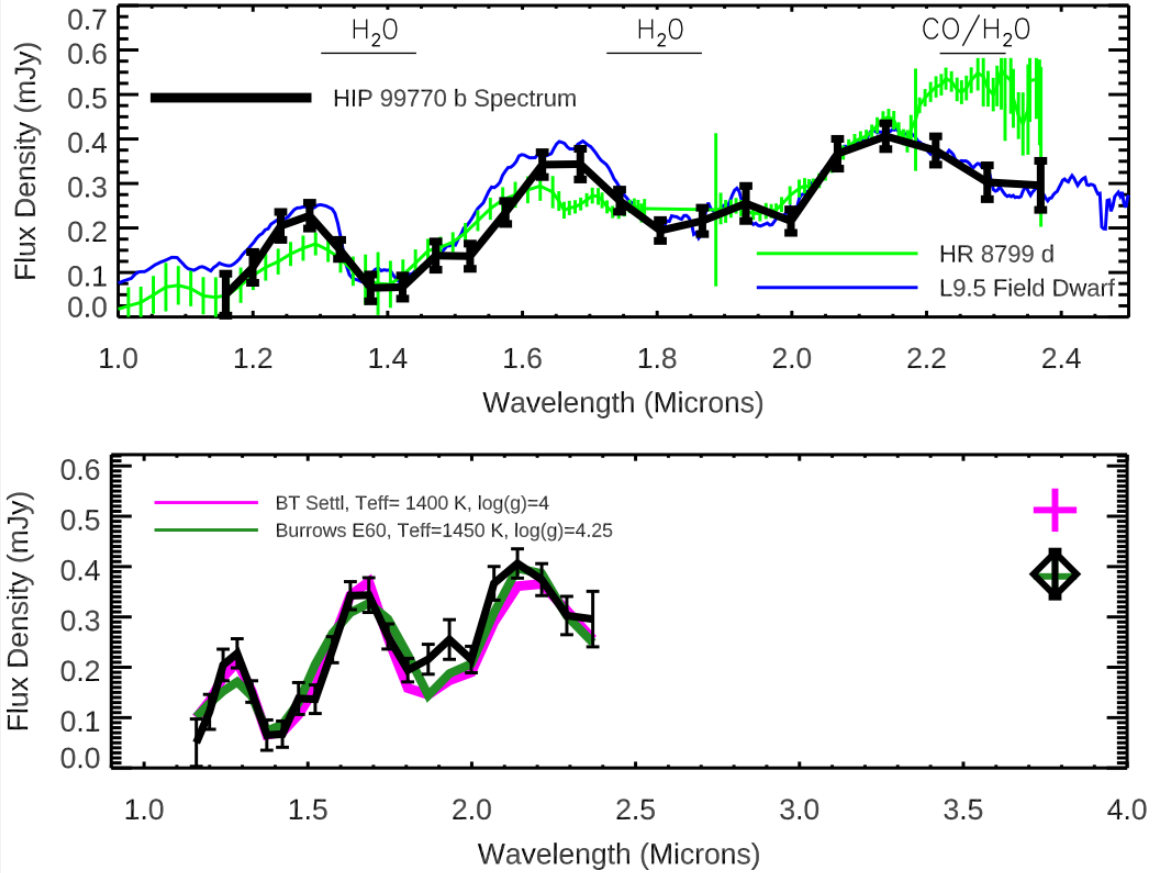


Figure 4: (top) HIP 99770 b spectrum compared to spectra for HR 8799 d extracted from GPI and SPHERE data (36, 37) and the L9.5 field dwarf SIMPJ0956-1447 drawn from the Montreal Spectral Library. The HR 8799 d and SIMPJ0956-1447 spectra are normalized to HIP 99770 b's at $2.1 \mu m$. We overplot regions of the spectrum shaped by absorption due to water and carbon monoxide. (bottom) HIP 99770 b's spectrum (black line) and photometry (black diamond) compared to representative, well-fitting atmospheric models from the BT-Settl and Burrows grids ($\chi^2_\nu = 1.35$ and 1.52 , respectively) (38, 39). The best-fit radii and implied masses are $0.92 R_J$, $3.3 M_J$ and $0.84 R_J$, $4.8 M_J$, respectively. Both models include clouds; the Burrows models include non-equilibrium carbon chemistry.

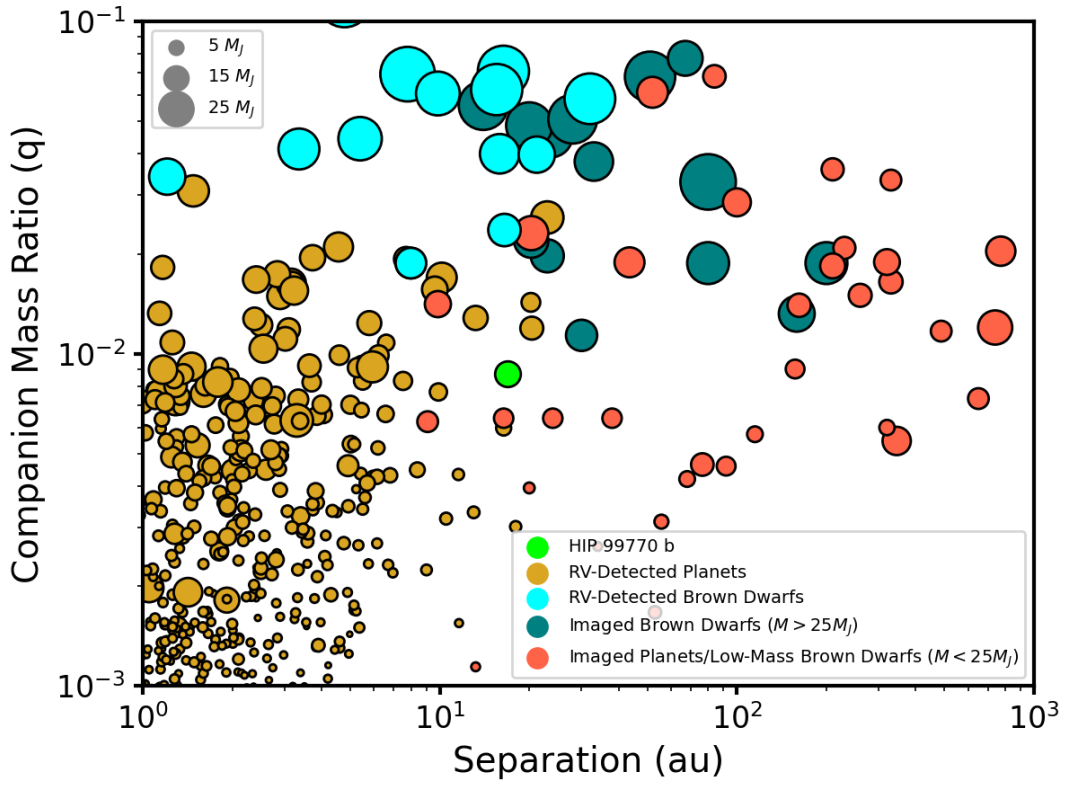


Figure 5: Mass ratio vs. separation for directly imaged exoplanets and brown dwarfs and RV-detected planets compared to HIP 99770 b. Symbol sizes are proportional to planet mass. Data are drawn from the NASA Exoplanet Archive and exoplanet.eu with small modifications. HIP 99770 b lies well within the region contiguous with RV-detected and directly-imaged exoplanets.

Supplementary Materials:

Supplementary Text

Figures S1 to S6

Tables S1 to S2

References (39-109)

Supplementary Materials

Systems Properties: HIP 99770’s spectral type and temperature estimates have a complicated history. Earlier studies classified HIP 99770 A as an A0V–A2V star based primarily on its weak metal lines (40). Complicating its spectral classification, HIP 99770 is long known as a λ Boo star whose spectrum is depleted in metals (41, 42). Its Balmer sequence is best fit by a mid A star, and the star’s most recent spectral type is listed as kA1.5hA7mA0.5 (30). The star’s λ Boo status therefore explains its weak metal lines, though weak metal lines are not necessarily indicative of an overall low bulk metallicity.

The star has $V-K_s = 0.518$; Gaia eDR3 data yield $M_G = 1.84$; $B_P-R_P \sim 0.26$ (16). These values are significantly redder than expected for an A0–A2 star. Using $V-K_s$ to estimate reddening (43, 44), the star’s implied reddening is $E(B - V) = 0.17, 0.12, 0.10$ and 0.03 for A0, A2, A3, and A5 spectral types. Values for HIP 99770’s $E(B-V)$ vary significantly in the literature, where the most recent values range from 0.014 to 0.025 (30). The star shows Na absorption consistent with cloud/dust absorption at a level of $E(B-V) \approx 0.02$ (45). To estimate credible values for reddening, we used a catalogue (kindly provided by E. Mamajek) that cross-references the Reis et al. (46) data with *Gaia* photometry. Within 50 pc and within 20° of HIP 99770, the median $E(B-V)$ is close to 0 with a maximum of $E(B-V) \sim 0.03$. Across all directions, the maximum is 0.05 . Separately, Murphy et al. (30) find a best-fit temperature of $T_{\text{eff}} \sim 7960$ K consistent with an A5–A6 star reddened by a small amount ($E(B-V) \sim 0.02$) but inconsistent with temperatures characteristic of early A stars (44).

We therefore adopt a temperature of $T_{\text{eff}} = 8000$ K and a spectral type matching this temperature: A5–A6. Using a M_V to luminosity relationship (44) we infer an apparent luminosity of $13.86 L_\odot$ and a mass of $1.84 M_\odot$. Adopting instead a luminosity from a standard mass-luminosity relationship and using the mass range of 1.7 – $2.0 M_\odot$ (31), we get a consistent value of $L_\star = 8.4$ – $16 L_\odot$.

HIP 99770’s age diagnostics lead to seemingly conflicting conclusions. On one hand, the star shares kinematics consistent with members of the ≈ 40 Myr-old Argus association (47, 48). Its space motion is an excellent match to the mean UVW velocities for the Argus core. While the star’s XYZ separation from the Argus core is ~ 80 pc, other members listed by Zuckerman et al. (48) are more separated, so it is not strictly speaking an outlier. *Banyan*- Σ analysis (23) updated with *Gaia* astrometry but not including photometry yields a 99.7% likelihood that HIP 99770 is an Argus member. Thus, the evidence for HIP 99770’s kinematic membership in Argus is strong but not decisive.

On the other hand, the star’s HR diagram position suggests an age older than Argus members, between that of the Pleiades and Ursa Majoris (115 Myr and 414 Myr, respectively (31, 49)) (Figure S1). HIP 99770 has a rotation rate of $v \sin i \sim 65$ km s $^{-1}$ (32): if viewed at a significant inclination angle – i.e. closer to pole-on – the star’s bolometric luminosity can be far lower than its apparent luminosity as was found for κ And (50), moving its HR diagram position away from Ursa Majoris and much closer to the Pleiades sequence or possibly even below. Follow-up CHARA interferometric data can better constrain the star’s polar angle, radius,

true luminosity, and therefore age.

An independent stellar age can be calculated using asteroseismology. HIP 99770 pulsates as a δ Sct star, a class for which asteroseismic ages have recently become feasible (51). Regular patterns are observed in the pulsation frequencies of young δ Sct stars (52), with a characteristic “large spacing” ($\Delta\nu$) that corresponds to the square root of the mean stellar density, i.e. $\Delta\nu \sim \sqrt{\bar{\rho}}$. As the star ages, its mean density decreases, and so too does its $\Delta\nu$. We used TESS data from Sectors 14 and 15, taken at a 2-min cadence, to construct an échelle diagram following (52). We measure $\Delta\nu = 4.86 \pm 0.03$, which suggests a much lower density than a typical slowly rotating δ Sct star near the ZAMS (e.g. Pleiades δ Sct stars have $\Delta\nu \sim 6.90$, (53)). We consider that this low density probably arises from centrifugal deformation due to rapid rotation, which can reduce the mean density by 37% for a star rotating at 2/3 of its break-up velocity (53).

To evaluate the implications for the age of HIP 99770, we constructed rotating stellar models for a mass of $1.8 M_{\odot}$, a solar metallicity ($Z = 0.0144$; (54)), and a range of uniform initial rotation rates, v_{in} . These correspond to: an equatorial viewpoint ($v_{\text{in}} = v \sin i = 65 \text{ km s}^{-1}$); a coplanar viewpoint ($i = 32^\circ$, $v_{\text{in}} = 122 \text{ km s}^{-1}$); the 8th decile of the rotational velocity distribution for mid-A stars from (32), being $v_{\text{in}} = 240 \text{ km s}^{-1}$ and implying $i = 16^\circ$; and a model at 280 km s^{-1} , whose rotation is so rapid as to delay the pre-MS contraction – this model eventually reaches 99.6% of its break-up velocity at age 100 Myr. The results are shown in Figure S2. The asteroseismological data are inconsistent with an equatorial viewpoint for HIP 99770 (blue) and also with a coplanar viewpoint (orange), both of which imply a density higher than that observed. Conversely, the inferred density is too high for HIP 99770 to be rotating at the limit of break-up (red). An age of ~ 180 Myr, slightly older than the upper limit of the Pleiades age, is found if the star is rotating uniformly at 240 km s^{-1} (green). Our calculations suggest a rotation rate of 180 km s^{-1} would be consistent with a UMa age of ~ 414 Myr (not shown).

Considering all lines of evidence, we adopt a bimodal distribution for possible ages: 40 Myr (based on Argus membership) or 115–414 Myr (based on the star’s HR diagram position and asteroseismology). Despite HIP 99770 A’s kinematics suggesting Argus membership, we favor the latter, older age range given the difficulty in reconciling the star’s internal density with younger ages. Furthermore, as we find below, an age of 115–200 Myr provides a self-consistent picture given the star’s properties and the age range consistent with HIP 99770 b’s luminosity and dynamical mass (see HIP 99770 b Luminosity). An interferometric measurement of the star’s rotation rate or inclination will allow a more precise age determination.

From the *Spitzer Heritage Archive* (SHA) and the *WISE* mission database, HIP 99770 shows no clear evidence for infrared excess at $\lambda < 22 \mu\text{m}$ consistent with warm circumstellar dust. However, HIP 99770 may be very marginally detected from a visual inspection of MIPS $70 \mu\text{m}$ data (taken on 20041016, PI M. Jura) and clearly seen in *Herschel Space Observatory* PACS $70 \mu\text{m}$ data (20120411, PI S. Molinar) with a flux density reported from the SHA of $157.5 \text{ mJy} \pm 11.8 \text{ mJy}$ (Figure S3). At $70 \mu\text{m}$, HIP 99770 A should have a flux density of $\approx 12 \text{ mJy}$, implying an observed to photospheric flux ratio of ≈ 13 , similar to stars with bright cold debris disks like AU Mic and PZ Tel (55). Assuming blackbody dust emission from a ring peaking at

$\lambda > 70 \mu m$, HIP 99770’s debris disk is colder than $\sim 40 K$ and at least 150 au ($3.7''$) in radius.

High-Contrast Imaging Observations and Data Reduction: We observed HIP 99770 as a part of our pilot accelerating star survey carried out with Subaru/SCEXAO (28). Table S1 summarizes our HIP 99770 high-contrast imaging observations. Typically, the seeing as measured in V band was slightly poorer than the Maunakea median value ($\sim 0.6''$). The June 2021 Keck data were of the highest quality, with excellent seeing ($\theta = 0.3''$ – $0.45''$), low winds, and extremely low precipitable water vapor ($PWV < 1$ mm). Similarly, the May 2021 SCEXAO observations typically had superb conditions, including extremely low winds, resulting in an exceptionally long atmospheric coherence time: a circular dark hole was visible in each CHARIS wavelength slice. However, the data periodically suffered from “low-wind effect” (56), leaving us with 39 minutes worth of data, slightly less than half of the original amount. Conditions for October 2021 were poorer than May/June 2021 but superior to those for other data sets and extremely stable. We measured an H band Strehl ratio of ~ 0.80 at the start of the July 2021 sequence. Raw contrasts were comparable or slightly better for the October 2021 data, while they were ~ 2 – 3 times deeper for the May 2021 data, similar to prior performances where the H band Strehl ratio measured 0.90–0.95 (57, 58).

To better remove stellar halo light, we obtained all observations in *angular differential imaging* (ADI) mode, allowing the sky to rotate, while keeping the telescope pupil fixed on the detector (34). The CHARIS integral field spectrograph data also enabled *spectral differential imaging* (SDI) (35, 59). For CHARIS, we utilized satellite spots produced by a 25nm sine wave modulation on the SCEXAO deformable mirror for precise astrometric and spectrophotometric calibration (60). To calibrate NIRC2 photometry, we took unsaturated images of HIP 99770. The CHARIS and NIRC2 data utilized a Lyot coronagraph with an occulting mask of $0.139''$ and $0.3''$ in radius, respectively.

To extract CHARIS data cubes from raw data, we used the standard CHARIS pipeline (61). We utilized the CHARIS Data Processing Pipeline (DPP) (58) for subsequent reduction steps: i.e. sky subtraction, image registration, spectrophotometric calibration, spatial filtering, PSF subtraction, throughput correction, and spectral extraction. To process NIRC2 data, we used a well-tested general use imaging pipeline (62), which performed comparable reduction tasks.

For PSF subtraction, we used the *Adaptive, Locally Optimized Combination of Images* (ALOCI) in combination with ADI or ADI+SDI (33, 63). We explored a wide range of algorithm parameter space. This meant varying parameters such as the *singular value decomposition* (SVD) cutoff, the number of N best-correlated frames included in the reference library, the rotation gap (δ), the subtraction/optimization zone geometries, and the use/disuse of a pixel mask over the subtraction zone (63–65), etc.

Figure S4 shows a gallery of our detections in each epoch. In the highest-quality data (October 2021 and May 2021), HIP 99770 b is detected at a signal-to-noise ratio (SNR) of $SNR = 39$ – 45 . For data processed utilizing ADI only and taken under the best conditions – May/October 2021 for CHARIS and June 2021 NIRC2 – HIP 99770 b is easily detected over the entire ALOCI parameter space explored, peaking at $SNR = 24.9$ for the October 2021 data. As a separate comparison for select CHARIS data, we also detected HIP 99970 b using an aggressive

implementation of the *Karhunen-Loève Image Image Projection* (KLIP) algorithm (66) with ADI: SNR = 17.8 for the October 2021 data. For October 2021 data reduced using ALOCI-ADI or KLIP-ADI, the final, sequence-combined PSF subtracted cubes revealed HIP 99770 b in every single CHARIS spectral channel. Utilizing SDI yielded an additional factor of 1.8–2.3 gain in SNR in the final ALOCI reductions.

To estimate and correct for spectrophotometric and astrometric biasing due to processing, we followed standard forward-modeling methods (57, 67), comparing the input and output flux density in each channel and position in the wavelength collapsed images. We assumed an L7 dwarf template spectrum imputed into each sequence, although the spectral type had no effect on the forward-model for ADI-reduced data. The astrometric offset was small, typically ~ 0.05 – 0.25 pixels in both east and north. To be conservative, we primarily adopted astrometry from the ADI-only reductions since the astrometric biasing is independent of the input spectrum. Our astrometric error budget considers the intrinsic SNR of the detection, a systematic error of 1/4 pixel in the centroid position, and an uncertainty in the pixel scale and north position angle of 0.05 mas and 0.27° , respectively. We assessed any evidence for a shift in the CHARIS north position angle offset from previously determined values (57) by obtaining multiple contemporaneous CHARIS observations and some NIRC2 observations of HD 1160 to detect its companion (68), failing to find any such evidence. HIP 99770 b’s May–July 2021 CHARIS and June 2021 NIRC2 astrometry also show strong agreement.

We adopted the throughput-corrected spectrum from the October 2021 ADI-LOCI reduction, as it represents the highest SNR reduction without using SDI and yielded a planet detection in every CHARIS spectral channel. Following previous work (69), we computed the spectral covariance from these data. The covariance at HIP 99770 b’s position is dominated by spectrally and spatially uncorrelated noise ($A_\delta \sim 0.88$). Spectra extracted from the May 2021 ALOCI-ADI and October 2021 KLIP-ADI reductions also show strong agreement over most channels (Figure S5) but have lower SNRs and stronger off-diagonal terms in their covariances leading to greater spectroscopic uncertainties.

Archival Data: We searched for additional HIP 99770 data that could possibly reveal a predisccovery image or otherwise constrain properties of HIP 99770 b. Despite being a bright young star, HIP 99770 was not targeted by either the *Gemini Planet Imager* survey (GPIS) or by various surveys with VLT/SPHERE, likely because of its low elevation/high airmass as seen from Cerro Pachon and Cerro Paranal. A search through the Keck Observatory Archive and Subaru Telescope Archive reveals no additional high-contrast imaging data sets.

However, HIP 99770 was targeted as a part of the *International Deep Planet Survey* (IDPS), observed in the CH_4 filter ($\lambda = 1.63 \mu m$) in Fall 2008 with the NIRC2 camera on Gemini North telescope (70), though contrast curves and a list of point sources detected were not published. If a background object, HIP 99770 b would appear at a position of $[E, N] \approx [-0.6, -1.23]$ at a contrast of $\approx 1.5 \times 10^{-5}$, which should be detectable from these data. To reinvestigate these data, we rereduced them using an updated *Julia* language *SNAP* pipeline (71). The NIRC2 data are saturated/non linear interior to $0.5''$ – $0.75''$. While *SNAP* achieves a contrast sufficient to recover HIP 99770 b if it were a background object at $\rho > 0.75''$ (1.2×10^{-5}), we fail to see it

in these data. The non-detection of HIP 99770 b in the NIRC2 data also rules out a small number of high eccentricity, high-mass orbital solutions.

Astrometric Modeling: Our joint modeling of HIP 99770 A’s absolute astrometry and the relative astrometry of HIP 99770 b includes the following steps. The Markov chains were comprised of 100 walkers taking 150,000 steps with 20 temperatures in parallel. We thinned the chains by a factor of 50 and discarded 75,000 steps as burn-in.

We explored the sensitivity our results had to input priors for the stellar mass and planet mass. For the stellar mass, we adopt a gaussian prior and changed the peak and standard deviation. For the planet mass, we performed fits both with a uniform prior (our nominal case) and a $1/M_p$ prior.

Table S2 shows our results. The covariances between the stellar mass and planet mass are weak. Increasing (decreasing) the prior peak value from $1.8 M_\odot$ to $1.9 M_\odot$ ($1.7 M_\odot$) results in only a 3% increase (4.4% decrease) in the median of the planet mass posterior distribution. Changing the width of the prior distribution has no effect on the planet mass. Adopting a $1/M$ prior on the planet mass leads to a posterior with a median value smaller by $\sim 15\%$: $13.9 M_J$. This shift is less than the $1-\sigma$ error on the inferred mass.

We also investigated the log likelihood ($\ln \mathcal{L}$) of the orbit as a function of companion mass drawn from our posterior distribution. The log likelihood peaks at $\approx 15\text{--}17 M_J$, and the upper envelope of the distribution drops by $\Delta \ln \mathcal{L} \approx 4$ at $4 M_J$ and $30 M_J$: orbits with a companion mass at the median of the posterior distribution fit the data best. Finally, we re-ran our simulations, doubling the astrometric errors in each epoch, effectively making the CHARIS astrometry uncertain to within 50-60% of a pixel in each coordinate for each epoch and the NIRC2 astrometry uncertain by 1.2 pixels in each coordinate. These errors are significantly larger than those we empirically estimated by comparing astrometry determined from different reductions for each data set (e.g. ADI vs ASDI reductions of CHARIS data: $\sim 2\text{--}3$ mas). The companion mass posterior is $17.5^{+8.7}_{-5.4} M_J$ in this case: less precise but otherwise indistinguishable from our other results.

Spectral Analysis and Atmospheric Modeling: HIP 99770 b’s near-IR colors provide a first, coarse context for the object’s atmosphere within the context of field and young brown dwarfs and directly-imaged exoplanets. As shown in Figure S6 (left), HIP 99770 b lies close to the color-magnitude diagram position of HR 8799 cde and young/field brown dwarfs near the L/T transition. Of the Figure S6 spectral standards derived in Currie et al (57) and derived from Cruz et al. (24), HIP 99770 b’s spectrum best matches an L7 spectral type (right panel).

We then compared CHARIS JHK spectra and NIRC2 L_p photometry to the library of empirical spectra from the Montreal Spectral Library. The empirical library covers field and young substellar objects ranging from early M to T spectral types: we focus solely on comparing their JHK spectra to CHARIS values. We find that HIP 99770 b is best matched by objects at the L/T transition (Figure S7), specifically an L9.5 dwarf. Then we compare HIP 99770 b’s CHARIS spectrum and NIRC2 photometry to atmosphere models derived from the BT-Settl grid and models from A. Burrows (39, 62, 72). The BT-Settl atmosphere models adopt the Asplund et al. (54) abundances. The BT-Settl include a self-consistent model for clouds and

dust entrained in clouds. The Burrows models either parameterize clouds via a shape function that describes the cloud truncation relative to the scale height of the gas or adopt cloud-free atmospheres. From this model family we consider the cloud-free model grid and the following cloudy models (ordered from least to most cloudy): E, AEE, AE, and A models. Following previous work, we vary the modal size of silicate dust in the atmospheres, from $30 \mu m$ to $100 \mu m$. Finally, we consider the influence of non-equilibrium carbon chemistry.

As in prior work (57), we focus only on the CHARIS channels unaffected by telluric absorption. We define the fit quality for the k th model using the χ^2 statistic, considering the spectral covariance:

$$\chi^2 = R_k^T C^{-1} R_k + \sum_i (f_{phot,i} - \alpha_k F_{phot,ik})^2 / \sigma_{phot,i}^2. \quad (1)$$

The vector R_k is the difference between measured and predicted CHARIS data points ($f_{spec} - \alpha_k F_{spec}$) and C is the covariance for the CHARIS spectra. The vectors $f_{phot,i}$, $F_{phot,ik}$, and $\sigma_{phot,i}$ are measured photometry, model predicted photometry, and photometric uncertainty. The scaling factor α_k minimizes χ^2 for a given model. From this scaling factor, we compute the planet radius, assuming a distance of $40.74 pc$.

The models used to infer HIP 99770 b’s atmospheric properties draw from two sources: 1) the BT-Settl grid (38) and 2) an updated version of the Burrows cloudy model grids, which are also used to generate predictions for Roman CGI passbands. Compared to previous publications (39, 72), the Burrows models are updated as follows. First, we incorporated molecular line lists from the Exomol collaboration (73, 74), which substantially changed the pressure dependence of water opacity critical for shaping the wings of HIP 99770 b’s spectrum (see Figure 4, top panel). Pressure dependencies for other molecules – e.g. metal hydrides, TiO – were likewise updated (75). Absorption cross sections for the strong resonance doublets of K and Na perturbed by H_2 collisions are incorporated using the results of (76) and (77) respectively. Compared to the previous-generation models, ours tend to be flatter/more blackbody-like for a given cloud/dust prescription.

Second, our models incorporate non-equilibrium carbon chemistry. Specifically, we define a boundary in temperature, T_Q , at which the mole fractions of CO/CH₄ are “quenched”. In other words, molecules at temperatures and corresponding pressures higher than this boundary are in equilibrium, at lower temperatures pressures chemical reactions operate as if the temperature is T_Q . This addition produces slight changes in the wings of synthetic spectra at H band and an increase in flux density at $2.2\text{--}2.4 \mu m$, both of which quantitatively improved our fits to HIP 99770 b spectra. We note that this treatment of non-equilibrium chemistry differs from the standard. T_Q is a free parameter directly, whereas in Hubeny & Burrows (78) and many other works considering non-equilibrium chemistry (e.g. (79)) the free parameter is an eddy-diffusivity value, K_{zz} which quantifies the strength of atmospheric mixing. The quench point is set to be the layer where the mixing timescale is equal to the chemical reaction timescale, with mole fractions of CO/CH₄ above this layer fixed to their values at the quench point, and mole fractions deeper than this layer in chemical equilibrium.

As noted in the main text, cloudy models with gravities and temperatures of $\log(g) = 4\text{--}5$

and 1300–1500 K reproduce most of HIP 99770 b’s spectrum and photometry. The best-fitting models from the Burrows grid assumes E-type clouds with a modal particle size of $60 \mu m$, a temperature of 1450 K . The goodness-of-fit is weakly dependent on surface gravity but slightly favors models with $\log(g) = 4.25$. These models imply radii that are ~ 20 – 25% smaller than those predicted for young jovians from evolutionary models (9, 80). The best fits for cloudier models require larger modal particles sizes ($100 \mu m$) and cooler temperatures ($\sim 1350 K$). These models have higher χ^2 , as their predicted spectra in J , H , and K are flatter than seen by HIP 99770 b. However, the implied radii are more consistent with evolutionary models ($R_p \sim 1 R_J$). Different prescriptions for clouds and dust or alternate opacities may improve fits. The HR 8799 planets show similar trends (62), where models with temperatures ~ 200 – $300 K$ lower but adopting improved cloud/dust prescriptions yield better agreement with data.

HIP 99770 b’s Luminosity: Given the possible ages of HIP 99770 b (40 Myr , 115–414 Myr) and HIP 99770 b’s luminosity of $\log(L/L_\odot) = -4.55 \pm 0.02$, hot start evolutionary models imply a mass of either $\sim 9 M_J$ or 11–32.5 M_J (80). HIP 99770 b’s range of radii and gravities from best-fitting models implies masses between 2.4 M_J and 39.5 M_J . Thus, direct dynamical mass measurements drawn from a small number of astrometric data points constrain HIP 99770 b’s mass with far greater precision than possible with either luminosity evolution models or atmospheric models.

HIP 99770 b’s luminosity is inconsistent with *cold start* luminosity evolution characterizing jovian planets formed with a low initial entropy but is consistent with *hot start*, high-entropy predictions (9). If hot start models – e.g. (80) – accurately predict the luminosity evolution of planets and brown dwarfs of a given mass, HIP 99770 b’s luminosity and dynamical mass combined strongly favor an age between 80 Myr and 200 Myr . Given our age estimate for the primary, the best supported age for HIP 99770 b would then be 115–200 Myr , which is consistent with an age derived from astroseismology if the star is a rapid rotator. Future data from facilities like CHARA will provide direct, more precise age estimates to compare with ranges expected given HIP 99770 b’s luminosity and dynamical mass.

Predictions for Roman-CGI: To predict the brightness of HIP 99770 b in the *Roman-CGI* passbands, we follow recent work extending the Burrows models to optical wavelengths (81). Briefly, we start with a small set of models from the Burrows grid primarily focusing on those covering the best-estimated temperature and surface gravity (Table 1). We consider best-fitting atmosphere models covering a range of cloud prescriptions and modal dust particle sizes, from E60 to AEE100 and AE100 and consider a fixed cloud/dust prescription with gravity varying from $\log(g)=4$ to 4.5. To estimate the contrast of HIP 99770 b in the optical for each of these models, we scale a suitable Kurucz atmosphere model to the star’s photometry. We update our method for generating optical spectra from those presented in Lacy & Burrows (81), using new line lists for sodium and potassium from the Exomol collaboration, which substantially affected the width of the sodium absorption feature centered on $\sim 0.59 \mu m$.

Figure S8 compares the contrast of HIP 99770 b to the primary star for five different models at 1450 K : 1) AE100, $\log(g) = 4$; 2) AE100, $\log(g) = 4$; 3) E60, $\log(g) = 4$; 4) E60, $\log(g) = 4.25$; and 5) E60, $\log(g) = 4.5$. At 575 nm where the CGI technological demonstration will

be performed, HIP 99770 b has a predicted optical contrast of 1.7×10^{-9} to 2.3×10^{-9} . While contrasts for the best-fit model (E60, $\log(g) = 4.25$; green curve) are likely beyond the reach of CGI, models with thicker clouds (AE100 and AEE100; black and magenta curves) yield contrasts comparable to those achieved in CGI laboratory tests ($\sim 10^{-9}$; bottom horizontal dashed line), because the presence of clouds moves the photosphere higher up in the atmosphere resulting in less pressure broadening of the major absorption sodium feature. In passbands covered by CGI’s long-slit spectrograph, contrasts are significantly milder, from $\sim 10^{-8}$ to CGI’s baseline performance requirement of 10^{-7} (upper dashed line). Our astrometric modeling predicts that HIP 99770 b will be $\sim 0.3\text{--}0.35''$ from the star during the CGI technological demonstration phase. Thus, HIP 99770 b could potentially be a test of CGI’s performance limit at 575 nm and is especially well suited for exoplanet spectral characterization at longer wavelengths.

Interpreting HIP 99770 b: In addition to being the first exoplanet jointly discovered through direct imaging and precision astrometry, to our knowledge HIP 99770 b is also the first confirmed exoplanet discovered using astrometry at all. Most prior attempts using astrometry to discover planets around main sequence stars have led to claims later refuted, null detections, unconfirmed candidates, or brown dwarf/M dwarf companions instead (82–85). With few (possibly no) exceptions, all exoplanets with astrometric detections besides HIP 99770 b were first detected using other methods (e.g. (21, 86)).

Figure 5 in the main text compares HIP 99770 b’s mass ratio and separation to that of other directly imaged objects and RV-detected planets. For planets, we primarily rely on the NASA Exoplanet Archive database. The exoplanet.eu webpage catalogues objects up to $60 M_J$ as possible planets (or brown dwarfs).

We combine the two data sources and make several modifications and corrections. Chiefly, we revise upward the masses for imaged companions 1RXJ 1609 B, GJ 504 B, GSC 06214 B, HIP 78530 B, and HR 7329 B based on updated system ages (10, 87, 88). Similarly, we revise the mass for VHS 1256 B and κ And b to modern values (57, 89). For the HR 8799 planets, we adopt the dynamical mass of HR 8799 e of $9.6^{+1.9}_{-1.8} M_J$ as the mass for HR 8799 cde (21) and set the mass of HR 8799 b to be $6.3^{+1.4}_{-1.3} M_J$ as a compromise drawn from dynamical and luminosity evolution-derived values (1, 62, 90, 91). HD 206893 b is missing from the NASA Exoplanet Archive as a directly-imaged planet but is now added (92); the Archive’s listed mass for HD 100546 b is substantially overestimated and is now revised to $4 M_J$ (63). The Archive also retains LkCa 15 bc although these claimed companions have been refuted (93): they are removed from our sample. Finally, we revert the mass estimate of BD20 +2457 b to $21.4 M_J$ (94).

The RV planet population has an upper envelope of $q \sim 0.01\text{--}0.02$ from 1 to ~ 30 au with a slightly smaller number of companions with slightly higher mass ratios ($q \sim 0.01\text{--}0.02$). The two RV-detected planets with discrepant mass ratios have large errors on the mass ratio e.g. HD 66428 b). Multiple RV-detected planets have similar mass ratios/separations to HIP 99770 b. The poor RV sample completeness at $a_p > 10$ au means that many planets with comparable mass ratios/separations will likely be discovered through future observations: e.g. those that now just show long-term RV trends (95). The imaged brown dwarf companions HIP 75056

AB, HIP 74865 B, and HR 2562 B and planet/brown dwarf companion GJ 504 B have $q \sim 0.015\text{--}0.025$ (96–99) : i.e. at or slightly below the mass ratio turnover identified from analyzing large ensembles of companions (26), although some of these companions (e.g. HR 2562 B) have masses that are not well constrained as they are highly sensitive to the assumed system age and/or adopted luminosity evolution model. Besides those targets, the plot shows a clean lower limit of $q \sim 0.025$ for objects unanimously classified as brown dwarfs. The lowest any object more massive than $25 M_J$ extends is $q \sim 0.015$. HIP 99770 b – $q \sim 0.0087$, $a_p \sim 16.9$ au – lies well within the population defined by bona fide planets.

HIP 99770 b’s likely mass straddles the deuterium-burning limit, roughly $13 M_J$. Many early studies identify planets as objects with masses below the deuterium-burning limit based on criteria suggested in 2003 by the *International Astronomical Union’s Working Group on Extrasolar Planets* (WGEP). WGEP explicitly notes that this definition – written over 18 years ago – is a *working definition* only, not a normative statement. It is focused on interpreting detections around mostly Sun-like stars and free-floating objects only and can *evolve* as more companions are detected around different types of stars.

As more recent work has decisively shown, taxonomy based on deuterium burning is poorly motivated (100). It is also frequently, sometimes explicitly rejected in practice within the direct imaging community and in major exoplanet catalogues such as the *NASA Exoplanet Archive* and *exoplanet.eu*. Below we articulate the unworkability of deuterium burning as a discriminator between planets and brown dwarfs. Instead we consider demographically-driven diagnostics presumably connected to formation processes, specifically the companion mass ratio and separation (q and a_p) (101) and mass drawn from surveys sensitive to both superjovian planets and brown dwarfs (95, 102). While demographics yield only a statistical argument at high masses that an object is a planet or brown dwarf, HIP 99770 b is safely within the phase space dominated by planets.

On the theory side, deuterium burning is time, metallicity, and helium abundance dependent (100) and arguably does not identify a meaningful boundary for the evolution of low-mass objects at all (103). To wit, “[a]ssigning different names to objects above and below the deuterium burning limit would be equivalent to assigning high and low-mass stars different names because of the presence and absence of the CNO cycle.” (104). During first $\sim 5\text{--}10$ Myr, the critical time for setting the final mass of a jovian planet, the luminosities of objects up to $20 M_J$ are still dominated by Kelvin-Helmholtz contraction (100): it is extremely difficult to see how the ignition of deuterium could affect nebular gas accretion, let alone shut it off the moment $13 M_J$ of material is accreted. Objects in the $\sim 15 M_J$ range, comparable to HIP 99770 b’s best-estimated mass, do not burn deuterium at all for the first tens of Myr after formation, potentially implying that an object could literally transform from a planet into a brown dwarf well after it formed.

On the observational side, recent imaging surveys have identified objects that are members of quadruple systems, clearly formed by molecular cloud fragmentation (i.e. like stars), with inferred masses down to $5 M_J$: some free-floating objects have sub-deuterium burning masses as well (105, 106). RV surveys have identified some systems – e.g. the $2.7 M_\odot$ star ν Oph – with

companions at ~ 1 au with masses of 22 and 24 M_J ($q \sim 0.008$ – 0.009) that are nevertheless locked in a mean-motion resonance indicating formation in a disk (i.e. as a planet) (107).

An alternate definition leverages on formation processes: a planet forms in a circumstellar disk around a young star. The demographics of substellar companion masses likely probe formation and provide another avenue for companion taxonomy. But they provide no basis for using the deuterium-burning limit to discriminate between planets and brown dwarfs, supporting (if anything) a substantially higher mass cutoff. Previous literature on the companion mass function for RV-detected companions with orbital periods less than \sim several years reaches a local minimum at minimum masses of $m \sin(i) \sim 20$ – $30 M_J$, not $13 M_J$ (102, 108–110), where objects less (more) massive than this limit are contiguous with a distribution drawn from Jupiter-mass (clearly brown dwarf) companions. As these are *lower* mass limits, the true minimum occurs at slightly larger masses. Furthermore, the minimum may be proportional to the primary mass, indicating that companion mass ratio – not mass – could be the primary discriminator (108).

To provide a modern investigation of the planet mass trends, we analyzed data drawn from the California Legacy Survey (CLS), an RV-survey with excellent completeness to superjovian-mass planets out to ~ 10 au (95). As shown in Figure S9, the CLS survey supports a minimum in $m \sin(i)$ of ~ 16 – $25 M_J$. Given the average expected line-of-sight inclination to these systems, the minimum in absolute mass is ~ 24 – $40 M_J$, about two to three times the mass of the deuterium-burning limit and significantly higher than HIP 99770 b’s dynamical mass.

As shown by several authors (62, 101), the semimajor axes (a_p) and mass ratios (q) of companions also provides a coarse diagnostic for distinguishing between bona fide planets and brown dwarfs. Protoplanetary disk radii span a range of values but their distributions peak at ~ 200 au and fall to low frequencies by ~ 300 au (111). While absolute values for disk masses rely on the gas-to-dust ratio and thus are uncertain by a factor of several, adopting solar values yields a median disk-to-star mass ratio $q_{disk} \sim 0.01$, where almost all disks have $q_{disk} < 0.1$ (112). Binary companions to more massive objects with mass ratios of $q \leq 0.05$ are exceptionally rare (113). Imaged objects with mass ratios of $q \leq 0.01$ – 0.02 and separations of $a_p \leq 200$ – 300 au roughly define a population contiguous with that of planets detected through indirect means.

As shown in Figure 5 of the main text, HIP 99770 b lies easily within the distribution of other companions widely acknowledged as planets. In practice, all of the objects labeled as planets by these criteria also have masses less than $25 M_J$.

An object’s orbital eccentricity may also diagnose formation mechanisms (11). Very low-mass planets like 51 Eri b or HR 8799 bcde have low eccentricities. Other companions – including those well above $30 M_J$ and $q \sim 0.02$ – have a broad range of eccentricities. HIP 99770 b’s low eccentricity is consistent with the planet population. As stated in the main text, HIP 99770 b receives roughly as much light as does Jupiter from the Sun.

Considered holistically, HIP 99770 b’s properties – insolation and mass ratio/separation, mass, and eccentricity compared those of other companions – clearly support interpreting it as a bona fide planet.

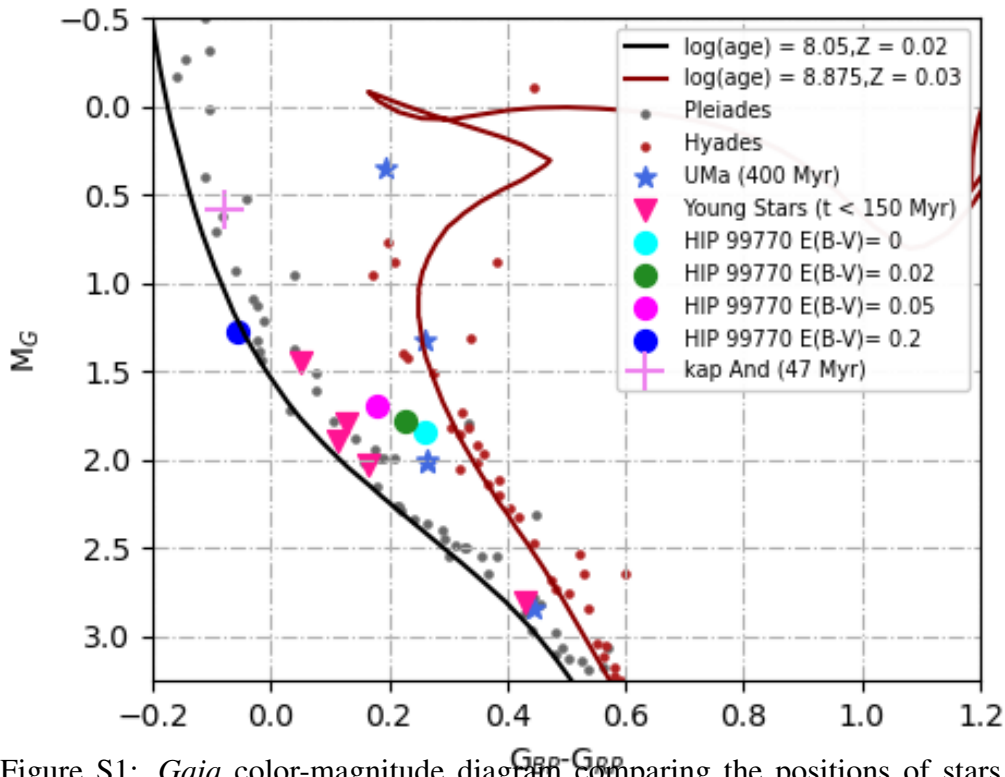


Figure S1: *Gaia* color-magnitude diagram comparing the positions of stars in the Pleiades (~ 115 Myr), Hyades (~ 750 Myr), isochrones for the Pleiades and Hyades, select Ursa Majoris stars with CHARA data (~ 414 Myr), and young stars with CHARA-estimated radii and ages with that for HIP 99770 under different assumptions about its line-of-sight reddening. Note that if HIP 99770 is viewed nearly pole on, its apparent luminosity can be significantly larger than its bolometric luminosity.

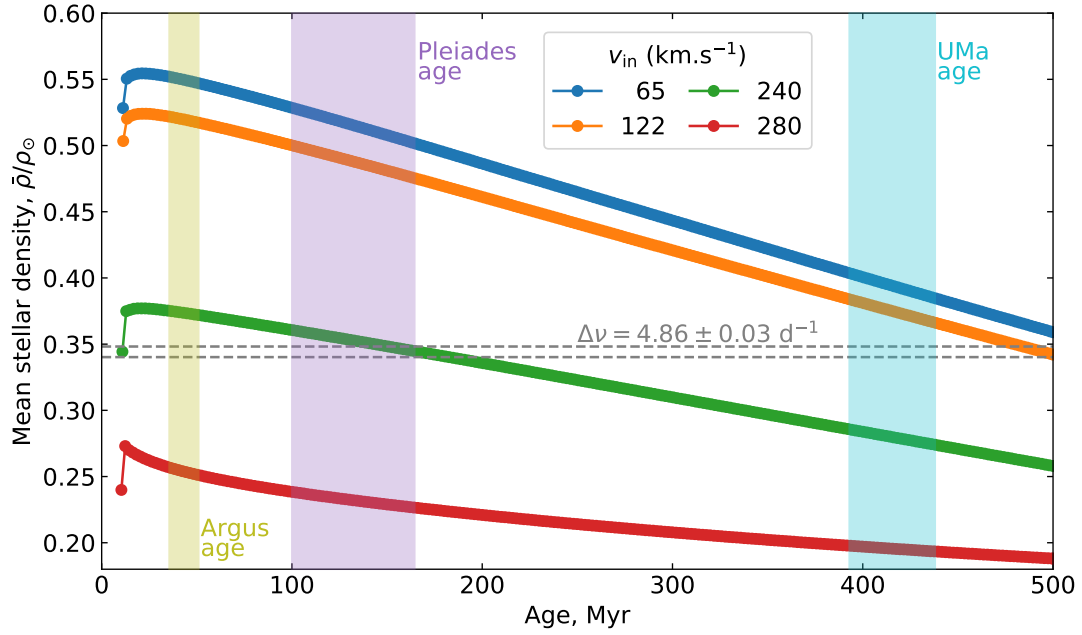


Figure S2: Mean stellar densities as a function of stellar age for four different rotation rates, sampled every 2 Myr from the end of the pre-MS (~ 10.5 Myr) to 500 Myr. Age ranges are shown for the Argus association (40 Myr; (48)), the Pleiades cluster (~ 115 Myr; see discussion in (53)) and the Ursa Majoris Moving Group (414 ± 23 Myr; (50)). The dashed grey line shows pulsation-derived density of $\bar{\rho}/\rho_{\odot} = 0.34$, corresponding to $\Delta\nu = 4.86$.

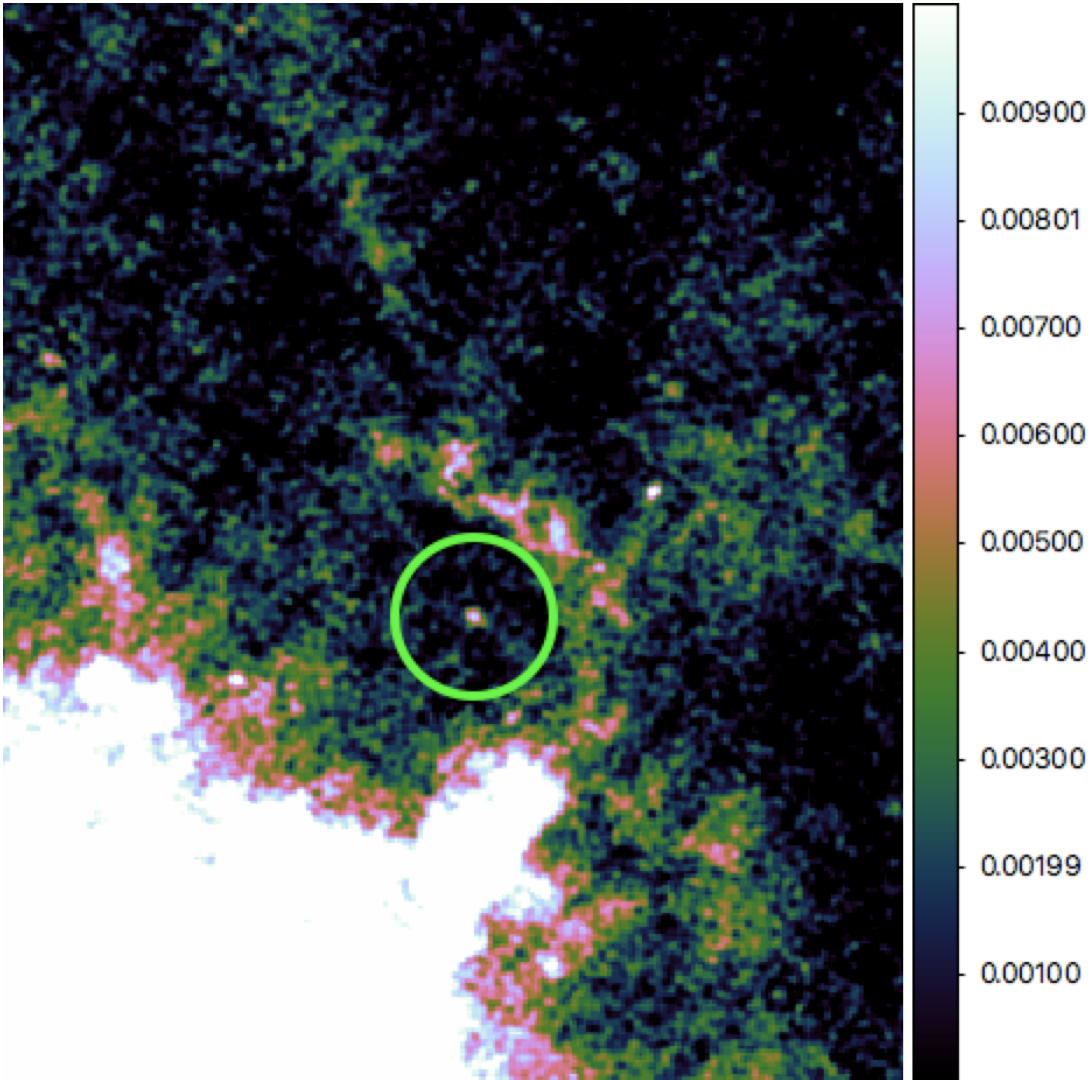


Figure S3: Detection of HIP 99770 in archival Herschel PACS 70 μm data: Herschel photometry suggest that HIP 99770 is surrounded by a luminous, Kuiper belt-like debris disk.

Table S1: HIP 99770 Observing Log

UT Date	Instrument	Seeing	Passband	λ (μm)	t_{exp} (s)	ΔPA ($^\circ$)
20200729	SCEXAO/CHARIS	0.7-0.8	<i>JHK</i>	1.16–2.37	1569	34.5
20200901	SCEXAO/CHARIS	0.7-1.1 ^a	<i>JHK</i>	1.16–2.37	2031	92.9
20210519	SCEXAO/CHARIS	0.3-0.5 ^b	<i>JHK</i>	1.16–2.37	2353	87.6
20210603	Keck/NIRC2	0.3-0.45	L_p	3.78	3750	61.9
20210713	SCEXAO/CHARIS	0.8-1.0	<i>JHK</i>	1.16–2.37	4337	62.5
20211017	SCEXAO/CHARIS	N/A ^c	<i>JHK</i>	1.16–2.37	5041	75.6

Notes - a) The original sequence was far longer: we removed 70% of frames suffering from periodically poor AO corrections due to variable seeing. b) While conditions for AO were superb, we chronically suffered “low-wind effect”, leading us to remove 60% of frames due to splitting/smearing of the PSF. c) No seeing estimate was available; raw SCEXAO/CHARIS contrasts were intermediate between July 2021 and May 2021 values.

Table S2: Astrometric Modeling Tests

Priors		Posteriors				
M_\star (M_\odot)	M_p (M_J)	M_\star (M_\odot)	M_p (M_J)	a_p (au)	i_p ($^\circ$)	e_p
1.8 ± 0.2	Uniform	$1.85^{+0.19}_{-0.18}$	$16.1^{+5.4}_{-5.0}$	$16.9^{+3.4}_{-1.9}$	148^{+13}_{-11}	$0.25^{+0.14}_{-0.16}$
1.8 ± 0.1	Uniform	$1.81^{+0.10}_{-0.10}$	$16.1^{+5.6}_{-5.0}$	$16.7^{+3.4}_{-1.7}$	149^{+12}_{-11}	$0.26^{+0.14}_{-0.16}$
1.8 ± 0.1	($1/M_p$)	$1.81^{+0.10}_{-0.10}$	$13.9^{+6.1}_{-5.1}$	$16.5^{+3.6}_{-1.6}$	151^{+12}_{-12}	$0.26^{+0.13}_{-0.16}$
1.7 ± 0.1	Uniform	$1.72^{+0.10}_{-0.10}$	$15.4^{+5.8}_{-4.6}$	$16.6^{+4.0}_{-1.9}$	151^{+13}_{-12}	$0.26^{+0.14}_{-0.15}$
1.9 ± 0.1	Uniform	$1.90^{+0.10}_{-0.10}$	$16.6^{+5.8}_{-4.9}$	$16.9^{+3.1}_{-1.7}$	146^{+11}_{-10}	$0.24^{+0.16}_{-0.16}$

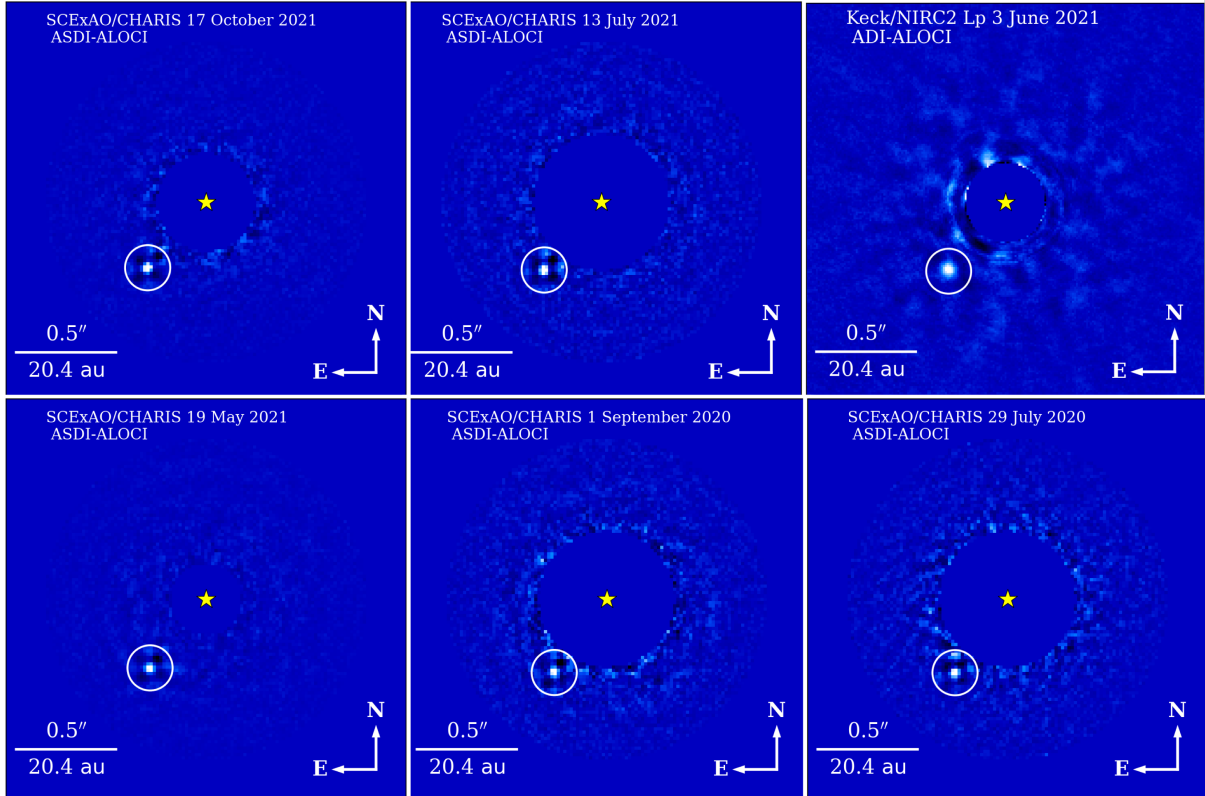


Figure S4: Gallery of highest SNR reductions for each epoch. We detect HIP 99770 b at SNR > 10 in each image.

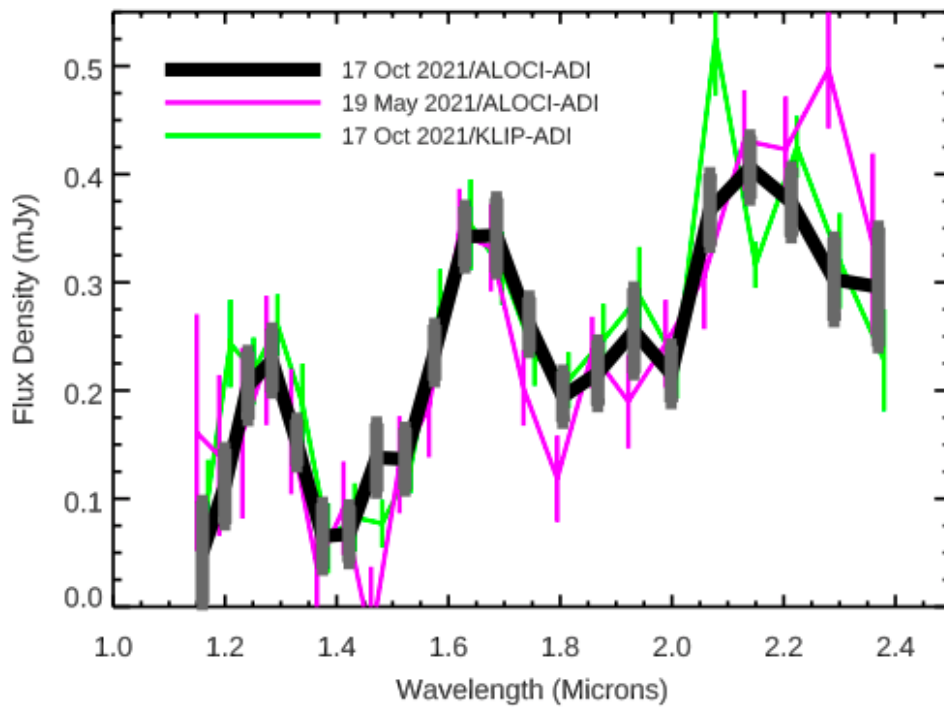


Figure S5: Our adopted HIP 99770 b spectrum (October 2021, ALOCI-ADI) compared to spectra extracted from May 2021 with the same algorithm (offset to the left in wavelength) or with a different PSF subtraction algorithm (KLIP-ADI; offset to the right in wavelength). The spectrum from May 2021 and the October 2021 spectrum obtained with KLIP-ADI both agree within errors to our adopted spectrum in 18 of the 21 spectral channels.

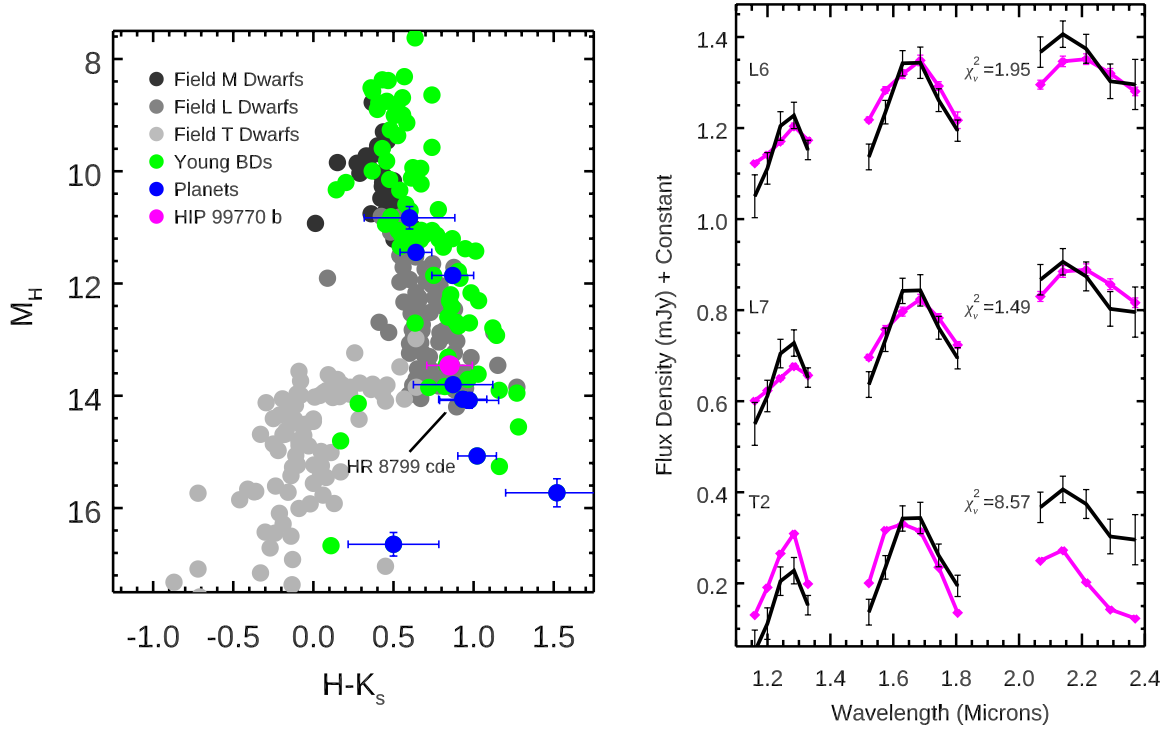


Figure S6: (left) Near-IR color-magnitude diagram comparing HIP 99770 b's photometric properties to field/young brown dwarfs and directly imaged planets. Data draw from Dupuy and Liu (114) with updated photometric entries for various planets. (right) HIP 99770 b's spectrum compared to spectral templates.

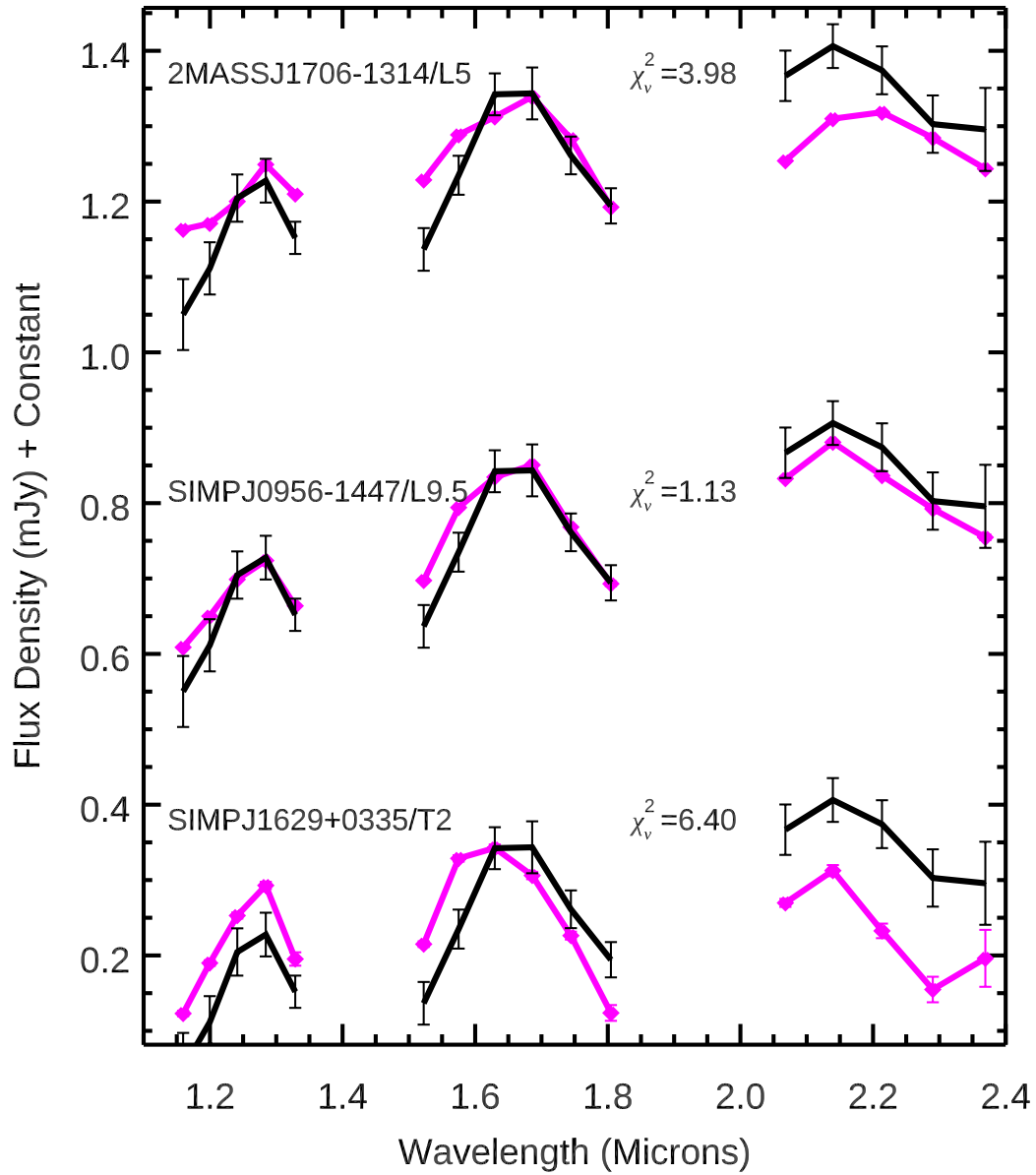


Figure S7: HIP 99770 b's spectrum (black line) compared to an L5, L9.5, and T2 dwarf drawn from the Montreal Spectral Library.

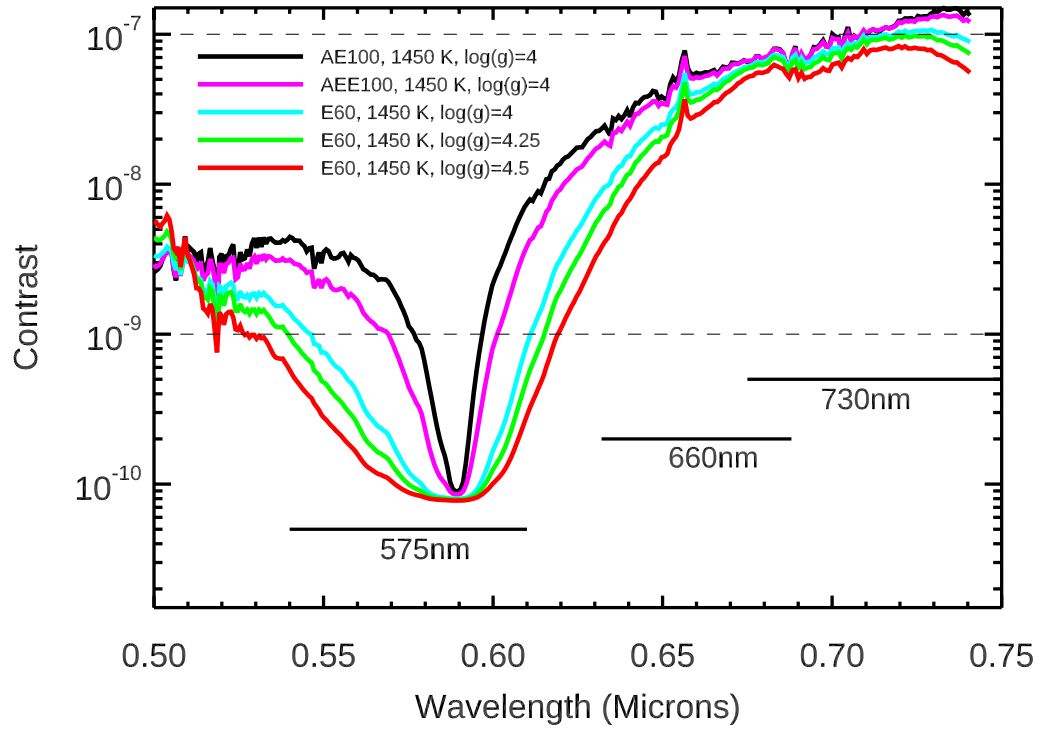


Figure S8: Predicted contrast between HIP 99770 b and its host star at optical wavelengths for different atmospheric models. The horizontal lines show the major CGI passbands for photometry used in its technological demonstration (575 nm) and spectroscopic bandpasses 660 nm and 730 nm. The top horizontal dashed line shows the notional CGI performance required for its technological demonstration; the bottom horizontal dashed line shows expected achievable contrasts for CGI should its flight performance match laboratory results.

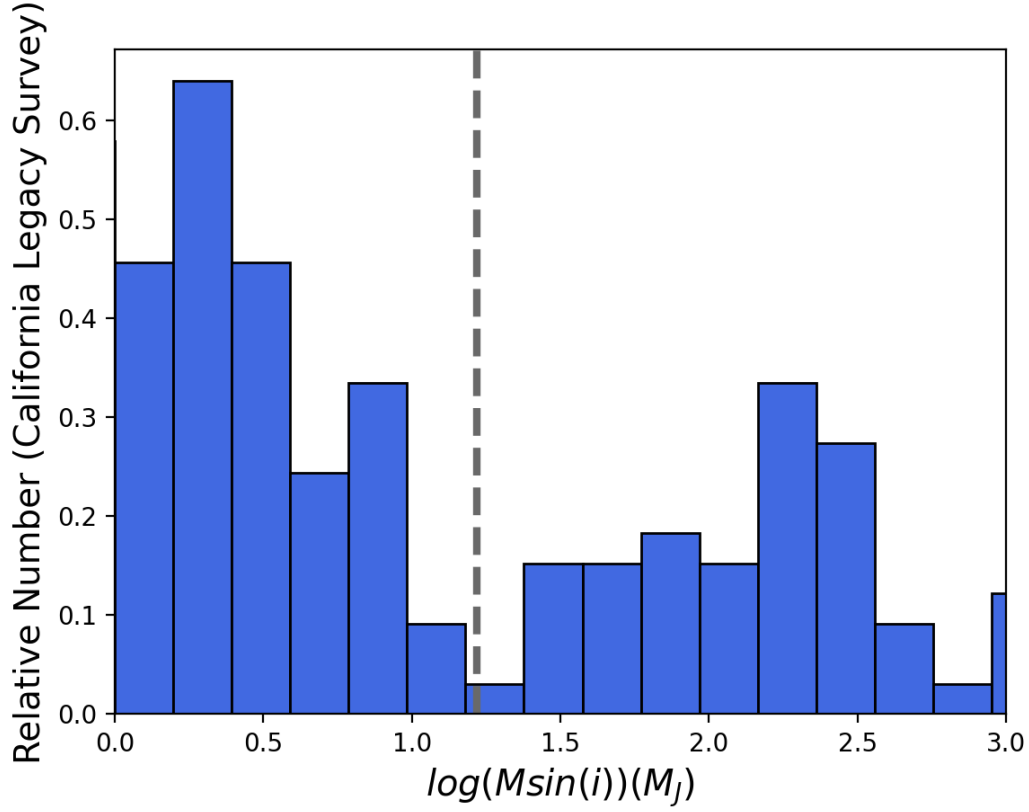


Figure S9: Histogram plot of the minimum mass ($m \sin(i)$) distribution from the California Legacy Survey for objects orbiting exterior to 0.1 au (i.e. those unaffected by irradiation and tidal disruption). The minimum occurs at $m \sin(i) \sim 16\text{--}25 M_J$. Considering inclination effects, the turnover in the companion mass function (nominally probing planets vs brown dwarfs) occurs at masses higher than that of HIP 99770 b (vertical dashed line).